

Lunar surface roughness derived from LRO Diviner Radiometer observations

Joshua L. Bandfield¹, Paul O. Hayne², Jean-Pierre Williams³, Benjamin T. Greenhagen², David A. Paige³

¹Space Science Institute

²Jet Propulsion Laboratory, California Institute of Technology

5 ³Earth, Planetary, and Space Sciences, UCLA

Manuscript Correspondence:

Joshua Bandfield
Space Science Institute
4750 Walnut Street, Suite 205
10 Boulder, CO 80301, USA

jbandfield@spacescience.org

Manuscript Pages: 39

Tables: 2

Figures: 15

Abstract

15 Sunlit and shaded slopes have a variety of temperatures based on their orientation with respect to the sun. Generally, greater slope angles lead to higher anisothermality within the field of view. This anisothermality is detected by measuring changing emitted radiance as a function of viewing angle or by measuring the difference in brightness temperatures with respect to observation wavelength.

20 Thermal infrared measurements from the Lunar Reconnaissance Orbiter Diviner Radiometer were used to derive lunar surface roughness via two observation types: 1) Nadir multispectral observations with full diurnal coverage and 2) multiple emission angle targeted observations. Measurements were compared to simulated radiance from a radiative equilibrium thermal model and Gaussian slope distribution model. Nadir observations most closely match a 20° RMS slope distribution, and multiple emission angle observations can be modeled using $20\text{--}35^\circ$ RMS slope distributions. Limited sampling

25 of the lunar surface did not show any clear variation in roughness among surface units. two-dimensional modeling shows that surfaces separated by distances greater than $0.5\text{--}5$ mm can remain thermally isolated in the lunar environment, indicating the length scale of the roughness features. Non-equilibrium conditions are prevalent at night and near sunrise and sunset, preventing the use of the equilibrium thermal model for roughness derivations using data acquired at these local times. Multiple

30 emission angle observations also show a significant decrease in radiance at high emission angles in both daytime and nighttime observations, and hemispherical emissivity is lower than is apparent from nadir observations. These observations and models serve as a basis for comparison with similar measurements of other airless bodies and as an initial template for the interpretation of TIR measurements acquired under a variety of geometric conditions.

Highlights

- 35 LRO Diviner thermal infrared measurements were used to derive lunar surface roughness
- Measurements indicate 20–35 degree RMS slope distributions at millimeter scales
- Lunar thermal emission is lower at high emission angles than nadir observations
- Anisothermality effects can dominate thermal and near-infrared planetary measurements

1. Introduction

40 1.1 Utility of roughness derivations

The development and reworking of the lunar surface is dominated by impact and space weathering processes, recording the history of the interaction between the Moon and the outside environment. By understanding this history, we can better understand surface processes on the Moon as well as other airless bodies within the Solar System. In addition, the surface layer is the principal factor influencing
45 most remote sensing measurements, and it is crucial to understand the relationship between the regolith at the surface and the primary materials from which it is derived.

Regolith properties, such as particle size distribution and density, represent a delicate balance of lunar surface processes that produce a highly structured regolith over time (e.g., *Keihm et al.*, 1973; *Vasavada et al.*, 2012; *Hayne et al.*, 2011; *Ghent et al.*, 2012). For example, overburden acts to
50 compress and increase the bulk density of the regolith, while small impacts have a tendency to disrupt the regolith locally, lowering its bulk density (*Bandfield et al.*, 2014).

There are few terrestrial analogs for the processes unique to the vacuum and space weathering environment and the resulting development of planetary surfaces. We can, however, rely on remote observations as well as samples and observations collected at lunar landing sites. Recent high
55 resolution imaging from the Kaguya, Chandryaan, Chang'E, and Lunar Reconnaissance Orbiter (LRO) spacecraft has provided a wealth of morphological data at a spatial sampling of down to ~0.5 m. However, outside of the few lunar landing sites that can be directly accessed, the vertical structure and sub-meter textures and heterogeneity of the lunar regolith must be characterized via alternate measurements and methods.

60 1.2 Measurements for roughness derivation

Large-scale lunar surface roughness (meter scales and greater) has been derived from laser altimetry and photogrammetry. The Lunar Orbiter Laser Altimeter (LOLA; Smith et al., 2010) on the LRO

spacecraft has been used to derive quantitative global slope information at decameter and larger scales (Rosenberg et al., 2011; Kreslavsky et al., 2013). In addition, digital terrain models derived from stereo
65 Lunar Reconnaissance Orbiter Camera (LROC; Robinson et al., 2010) and Selene Terrain Camera (Haruyama et al., 2006) images have been used to characterize lunar surface slopes at scales as small as 2 m (e.g., Manhanti et al., 2014). These studies have, for example, quantified differences in surface slope distributions between lunar highlands and maria, characterized crater shapes at a variety of scales, and documented the development of ejecta deposits with age (Rosenberg et al., 2011; Kreslavsky et al.,
70 2013; Manhanti et al., 2014).

Photometric (Hapke, 1984; Shkuratov et al., 2005) and *in-situ* (Gold, 1970; Lumme, et al. 1985; Helfenstein and Shepard, 1999) measurements have been used to characterize small-scale (centimeter scales and smaller) lunar surface roughness. Helfenstein and Shepard (1999) derived surface slope distributions from Apollo Lunar Surface Closeup Camera images at scales from ~0.1 to 85 mm, and
75 found average RMS slope angles of ~16–25° for the lunar regolith. These slope distributions are dominated by steep slopes at the smallest scale of measurement. Photometric observations derived similar values for lunar surface roughness (e.g., Helfenstein and Ververka, 1987; Helfenstein and Shepard, 1999; Goguen et al., 2010); however, these observations have shown a wide range of roughness values, and cannot confidently separate roughness from other factors such as porosity and
80 albedo (Shepard and Helfenstein, 2007; Goguen et al., 2010).

Radar measurements can be used to characterize the lunar surface roughness at centimeter to meter scales (e.g., Hagfors, 1967). Both surface roughness and subsurface heterogeneities cause increased radar backscatter that can be used to define and characterize lava flows, crater ejecta, and other features (e.g., Thompson et al., 1974; Ghent et al., 2005; Thompson et al., 2006; Campbell et al., 2009;
85 Campbell et al., 2010; Carter et al., 2012). Radar measurements are particularly sensitive to the presence of rocks at the surface and in the shallow subsurface, and have been used to better understand

lunar regolith development (e.g., Ghent et al., 2005).

1.3 Thermal infrared roughness measurements

Thermal infrared (TIR) measurements have been used to infer the surface roughness of the Moon and
90 other bodies such as asteroids, comets, and Mars (e.g., Sinton, 1962; Smith, 1967; Buhl, 1968; Spencer,
1990; Johnson et al., 1993; Jämsä et al., 1993; Lagerros, 1998; Bandfield, 2009; Davidsson et al., 2009;
Rozitis and Green, 2012; Groussin et al., 2013; Davidsson et al., 2013). Much of this work has focused
on producing a unitless “beaming” parameter to correct for surface roughness effects in order to derive
other properties, such as estimated sizes of the unresolved objects, with greater accuracy (e.g., Spencer,
95 1990).

Thermal infrared measurements are sensitive to surface roughness in two basic ways: 1) The relative
proportions of sunlit and shaded surfaces within the measurement field of view changes based on the
viewing angle. For example, a greater proportion of warm, sunlit surfaces contribute to the
measurement when viewing a rough surface from the same azimuth angle as the sun, resulting in a
100 warmer apparent temperature. 2) From a single viewing angle, both warm sunlit and cool shaded
surfaces contribute to the measurement. This mixture of temperatures will result in spectrally non-
uniform brightness temperatures with higher temperatures at shorter wavelengths. In general, the
greater the roughness of the surface, the more prominent these effects appear in the TIR data

Temperature measurements are sensitive to length scales at which surfaces can remain thermally
105 isolated. The scale of sensitivity is dependent on the thermal conductivity of surface materials and the
rotational and seasonal periods of the body, but is typically millimeter to meter scales. This bridges a
gap between sub-millimeter-scale roughness derived from photometry studies and larger scale slope
distributions derived from laser ranging and photogrammetry. TIR roughness determinations also
complement radar-based measurements that are sensitive to subsurface heterogeneities. In this manner,
110 TIR measurements can be used to derive surface information that can be directly related to the

properties of the lunar regolith, such as the development of surface textures with soil maturation.

Most roughness studies using TIR measurements have had to rely on unresolved whole-disk observations, and are often acquired over a limited time span. However, some work has been documented regarding the derivation of surface roughness properties from TIR measurements acquired
115 of a single surface from a variety of phase and emission angles (Winter and Krupp, 1971; Jakosky et al., 1990; Bandfield and Edwards, 2008). These spacecraft observations are able to systematically assemble a more complete emission phase function of planetary surfaces. These phase function observations not only provide a semi-independent means of determining surface roughness, but also provide important information regarding the radiative budget of planetary surfaces.

120 Thermal emission from the lunar surface is well known to be affected by surface roughness (Pettit and Nicholson, 1930; Sinton, 1962; Smith, 1967; Buhl et al., 1968; Winter, 1970; Winter and Krupp, 1971). Telescopic measurements showed that, for example full Moon measurements showed significantly more radiance at the limb than would be expected from a smooth Lambertian surface. This was generally attributed to preferential viewing of sunlit slopes due to small scale cratering (Sinton, 1962;
125 Buhl et al., 1968; Winter and Krupp, 1971). By contrast, Smith (1967) described roughness in a more generalized RMS slope distribution, though without attributing the roughness to any particular formation process.

1.4 Scope of work

Our goal is to model and derive lunar surface roughness using LRO Diviner Radiometer measurements.

130 We characterize the spectral phase behavior of lunar TIR measurements, and show that surface roughness can have significant and sometimes dominant effects on lunar TIR measurements. We also present a simple TIR roughness model for comparison to the Diviner measurements. This work is an initial exploration and characterization of lunar surface roughness and phase effects, and we investigate a limited number of sample regions. Systematic global mapping of surface roughness or a detailed

135 examination of the effects of specific surface slope distributions on measurements and models is
beyond the scope of our work as it is presented here.

2. Modeling

2.1 Thermal model

Our thermal model assumes radiative equilibrium to predict surface temperatures. Sloped surfaces
140 include a downwelling radiative component proportional to the fraction of the hemisphere filled by
adjacent surfaces rather than space. To maintain computational efficiency, the solar and thermal
infrared downwelling radiance is calculated assuming it is coming from a horizontal surface at radiative
equilibrium. The assumption of radiative equilibrium is appropriate for daytime surfaces of slowly
rotating bodies with low thermal inertia, such as the Moon. Under these conditions, heat diffusion
145 models predict equatorial surface temperatures within $\sim 1\text{K}$ of radiative equilibrium between 0800H and
1600H. This methodology is not appropriate for prediction of measurements at night or during rapidly
changing radiative conditions, such as near sunrise or sunset.

Where the solar incidence for a given slope angle is greater than 90° or for surfaces within cast
shadows (described below), the surface is set to 100K, consistent with nighttime temperature
150 measurements (e.g., Vasavada et al., 2012). In practice, the precise temperature of shaded surfaces
matters little for daytime measurements at thermal infrared wavelengths because the amount of
radiance is small relative to that from warm sunlit surfaces.

2.2 Surface roughness model

We use a simple Gaussian roughness model that is similar to that described by *Helfenstein and Shepard*
155 (1999) and has been used for comparison to martian TIR datasets (*Bandfield and Edwards, 2008;*
Bandfield, 2009). Surface temperatures are predicted for slopes of 0 to 90° at 2° intervals and azimuth
orientations of 0 to 360° at 20° intervals. The radiance of each slope/azimuth combination is calculated,
and its contribution to the total modeled radiance is weighted by the statistical probability of its

occurrence. This reduces the surface slopes/roughness to a single parameter (RMS slope) that is
160 independent of length scales while maintaining reasonable fidelity to natural surfaces.

The probability distribution P for a given slope angle, θ , is described by the following (derived from
Eq. 13 of Shepard et al., 1995):

$$P(\theta) = \frac{\tan(\theta)}{\tan^2(\theta_0)} \cdot e^{-\frac{\tan^2(\theta)}{2 \cdot \tan^2(\theta_0)}} \quad (1)$$

, where θ_0 is the tangent of the RMS slope angle. This describes the adirectional distribution of slopes,
which closely approximates a Gaussian distribution of unidirectional slopes for a RMS slope angle of
165 θ_0 (Shepard et al., 1995). For our purpose, the azimuth direction for the slope of any given surface has
no preferential orientation and our measurements are sensitive to an adirectional distribution of slopes
with random azimuths rather than the slope distribution along any particular transect or orientation.

Using the modeled temperatures and slope distributions, the mixture of Planck radiances are calculated
in proportion to their contribution to the measurement field of view based on the observation geometry.
170 For example, slopes facing away from the observer will contribute proportionally less to the
measurement than slopes facing the observer. This factor is calculated from the dot product of the
vector normal to the local surface and the observation vector.

Shadows greatly influence the emitted radiance from planetary surfaces at high angles of solar
incidence or where high slope angles are present. Although it is simple to predict whether a sloped
175 surface has a local solar incidence of greater than 90° , predicting the distribution of cast shadows on
slopes that would otherwise be sunlit is much more difficult and an exact solution requires ray-casting
and other computationally expensive methods.

We use a shadowing approximation methodology modified from that developed by *Smith* (1967) and
Hapke (1984). This model assumes that any slope/azimuth surface that would otherwise be illuminated
180 has the same statistical chance of being within a shadow cast by another surface. This is a relatively

simple approach for nadir observations described by the following (derived from Eq. 21 and 24 of *Smith, 1967*):

$$S(\theta) = \frac{[1 - \frac{1}{2} \operatorname{erfc}(\frac{\mu}{\sqrt{2}\omega})]}{\frac{1}{2} [\sqrt{(2/\pi)} \cdot \frac{\omega}{\mu} e^{-\mu^2/2\omega^2} - \operatorname{erfc}(\mu/\sqrt{2}\omega)] + 1} \quad (2)$$

, where $S(\theta)$ is the fraction of the shadowed surface, μ is the cotangent of the solar incidence angle, ω is the RMS surface slope distribution, and $\operatorname{erfc}(x)$ is the complementary error function (the integral between 0 and x of a Gaussian distribution function).

This equation can only be applied as is to nadir observations, where no surface is hidden from the spacecraft view (assuming no overhanging surfaces). For off-nadir observations, it is necessary to include a modification of Eq. (2) with a function that describes the abundance of cast shadows that are visible from the elevation/azimuth of the viewing platform. For example, when viewing a surface from the same elevation and azimuth as the sun, no shadowed surfaces will be visible even if shadowed surfaces might otherwise be visible from a nadir orientation (i.e., “shadow hiding”). To account for viewing orientation effects, we use an approach similar to that described by *Hapke (1984)*. Where the viewing emission angle is greater than the solar incidence angle, the shaded fraction observed at nadir, $S_{nadir}(\theta)$, is modified by the following:

$$S_{view}(\theta) = S_{nadir} \cdot (1 - e^{-2 \tan[\frac{1}{2}(\phi_{sun} - \phi_{obs})]}) \quad (3)$$

, where $S_{view}(\theta)$ is the fraction of shadowing that is present within the field of view, ϕ_{sun} is the azimuth angle of the sun with respect to the surface, and ϕ_{obs} is the azimuth angle of the spacecraft with respect to the surface. Where the viewing emission angle is less than the solar incidence angle, the following applies:

$$S_{view}(\theta) = S_{nadir} - S_{obs}(\theta) \cdot e^{-2 \tan[\frac{1}{2}(\phi_{sun} - \phi_{obs})]} \quad (4)$$

, where $S_{obs}(\theta)$ is the shadowing function described in eq. (1), except as applied to the viewing incidence angle of the spacecraft rather than the sun.

3. Diviner Data

3.1 Instrument description

The Diviner Radiometer has seven thermal infrared spectral channels; three spectral filters are near 8 μm wavelength and separate filters also cover $\sim 13\text{--}23$, $25\text{--}41$, $50\text{--}100$, and $100\text{--}400$ μm wavelengths (Paige *et al.*, 2010a). Each channel consists of a 1 by 21 element detector array, and separate spectral channels are arranged and data are typically collected in a nadir-pointing pushbroom configuration. The spatial sampling of each Diviner detector element at nadir is ~ 160 by 320 m from a 50 km polar orbit and the local time of observations migrated across the full diurnal cycle throughout the primary LRO mission. The two axis pointing capability of Diviner allows for collection of targeted observations and two point full-aperture calibration observations of space and a reference surface. More complete descriptions of the Diviner instrument characteristics and operations are given in Paige *et al.* (2010a; 2010b).

3.2 Datasets

3.2.1 Nadir observations

We selected four equatorial regions of interest (ROIs) for analysis using nadir-oriented Diviner measurements. These include dark mantled deposits in southern Sinus Aestuum (Gaddis *et al.*, 1985), cold spot surfaces (Bandfield *et al.*, 2014), and mare and highlands surfaces (Table 1; Figure 1). All data were acquired between June 2009 and March 2014 with emission angles of $0\text{--}5^\circ$. These ROIs were selected based on their relatively uniform terrain and large spatial extent to ensure well-sampled diurnal coverage. These ROIs are used for an initial analysis of several different lunar surface units and are not meant to serve as a comprehensive global analysis. All measurements from each orbit within the ROI were averaged, resulting in 122 to 733 data points for each spectral channel and full diurnal coverage for each region.

3.2.2 EPF observations

The two-axis pointing capability of Diviner allows for the collection of off-nadir targeted observations.

In addition to the typical nadir-oriented mapping observations, we include a limited set of targeted observations that were acquired over surfaces from a series of emission and azimuth orientations as the LRO spacecraft passed overhead. These observations are referred to as emission phase function (EPF) observations throughout this manuscript.

230 The EPF observations were collected from nine angles parallel to the LRO orbit track. Surface emission angles are $\sim 0, 53, 62, 69,$ and 76° , with observations collected both up- and down-track with respect to the spacecraft orbit, producing a series of measurements symmetrical with respect to the nadir observation. Sixty-four separate EPF sequences were acquired by Diviner between LRO orbits 4450 and 7398 at a variety of local times and equatorward of $\sim 70^\circ$ latitude. Of these, we selected six
235 EPF sequences that covered warm surfaces (local times between 0900H and 1500H and equatorward of 60°) with solar incidence angles exceeding 20° for comparison with the thermal roughness model (Table 2; Figure 1).

In addition, we also investigated 23 nighttime EPF sequences (Table 2; Figure 1). Our rough surface model cannot be accurately applied to the nighttime sequences because it assumes radiative equilibrium
240 and all surfaces would, as a result, be modeled at 0 K. However, we include these observations here for the purpose of documenting their temperature and radiative phase behavior.

Both the increased target distance and the oblique projection of the measurement field of view on the surface result in a much larger spatial sampling at increased emission angles. For example, from the 50 km LRO mapping orbit, surface sampling grows to ~ 650 by 5500 m at an emission angle of 76° . As a
245 consequence, useful observations are limited to relatively homogeneous areas. Similar EPF sequences were acquired by the Mars Global Surveyor Thermal Emission Spectrometer, and the variable spatial resolution and surface sampling did not prevent their use and the derivation of surface characteristics (Bandfield and Smith, 2003; Bandfield and Edwards, 2008).

3.2.3 Comparison of model with instrument data

250 In order to directly compare Diviner measurements with model results, it is necessary to account for instrument and environment characteristics. Modeled radiance is convolved with the Diviner filter bandpasses to produce integrated radiance values that are the equivalent of the Diviner calibrated radiance. These radiance values were converted to brightness temperature using a lookup table consisting of Planck radiance spectra convolved with each of the Diviner filter functions. In addition, 255 the solar band albedo values for modeled surfaces were derived from the average of the 0.45 μm and 0.75 μm Clementine global multispectral mosaic reflectance (Isbell et al., 1999). Although these data do not provide the precise value of the Bond albedo necessary to predict the surface temperature, our primary goal is to model temperature differences between different phase angles and wavelengths, rather than absolute temperatures. Small changes in albedo have little effect on these temperature 260 differences.

In addition, variable surface emissivity can cause significant variations in radiance between Diviner spectral channels. In order to determine surface emissivity for the nadir Diviner observations, we use nadir noontime equatorial observations. Modeling indicates that surface roughness has little effect where solar incidence is less than $\sim 30^\circ$, and these observations can be considered free of its interfering 265 effects (*Davidsson et al.*, submitted). Surface kinetic temperature is determined by assuming a maximum emissivity of 0.99 in Diviner Channels 3–5, consistent with laboratory thermal infrared reflectance spectra of lunar samples (*Salisbury et al.*, 1997). EPF observations, for our purposes, only require comparison between observations of the same spectral channel. In this case, we simply assume an emissivity of 0.99 for each spectral channel. Although spectral emissivity variations exist between 270 surfaces of different composition and maturity (e.g., Greenhagen et al., 2010), they are relatively subtle, and their effects are minimized when only comparing data from a single spectral channel over a given surface.

4. Results

4.1 Nadir observations

275 To characterize surface roughness using the nadir oriented measurements, we use all Diviner
wavelengths, but focus on brightness temperature differences between Diviner Channels 4 or 6 (8.2 or
12–25 μm) and 7 (25–41 μm). Channel 4 is typically at the peak of the Christiansen feature in Diviner
data (Greenhagen et al., 2010) and is less susceptible to emissivity variations than Channels 3 and 5
(7.8 and 8.6 μm respectively). Channel 7 was used because the long wavelengths relative to Channel 4
280 allows for anisothermality due to surface roughness to be detected readily, and these two channels are
nearly co-boresighted. The longer wavelength Channels 8 and 9 (50–100 and 100–300 μm) present
some difficulties because there is a potential source of extra radiance present at the hottest temperatures
(e.g., noontime equatorial observations) that interferes with the analysis.

The difference in brightness temperature between spectral channels provides an indication of the range
285 of temperatures within the measurement field of view. Surfaces that are nearly isothermal can be fit
well with a single Planck radiance function and will have similar brightness temperatures at all
wavelengths. By contrast, a rough surface and higher angles of solar incidence can result in a large
range of temperatures within the measurement field of view. Under these circumstances, the Planck
radiance function can only match the measured radiance at a single wavelength, with shorter
290 wavelengths requiring higher temperatures to fit the measurement.

All Diviner spectral data show a clear trend of increasing blue spectral slope with increasing solar
incidence angles for all four surface units (Figures 2 and 3). For example, near 1200H, Diviner
measured mare surfaces at 398K and 393K brightness temperatures in Channels 4 and 7 respectively.
By contrast, the same surface at 0630H had brightness temperatures of 249K and 205K. For the early
295 morning observations the brightness temperatures differed between short and long wavelengths by 44K
versus 5K for the noon time observations.

The nadir measurements for all four ROIs display surface temperatures similar to the equatorial surface temperatures analyzed by Vasavada et al. (2012). Peak noontime temperatures reach nearly 400K and drop to less than 100K at night (Figure 4). Diviner Channel 4 brightness temperatures are always
300 higher than the longer wavelength Channel 7 temperatures throughout the lunar day. From 0900H to 1500H, the Channel 4 brightness temperatures are 5–10K warmer for all surfaces and there is no clear systematic variation of anisothermality between 1000H and 1400H (Figure 2). With higher incidence angles closer to sunrise or sunset, the brightness temperature differences are much higher, commonly reaching 40K and above within an hour of sunrise or sunset. The degree of anisothermality is
305 significantly higher (commonly by 10–15K) just after sunrise compared to just before sunset.

There is no clear difference in the pattern of anisothermality throughout the lunar day between the four ROIs (Figure 2). The highlands and cold spot surfaces show a greater amount of scatter in their temperatures due to the regional topography of the highlands surfaces within the ROI. However, both locations show a pattern of increased anisothermality with increasing solar incidence similar to the dark
310 mantle deposit and mare surfaces.

For comparison of nighttime and full diurnal measurements, Channel 6 was used instead of Channel 4 (Figure 5). Channel 6 is the shortest wavelength measurement that can be used at night with adequate signal. All of the nadir-oriented ROIs have rock abundance values of <1% (Bandfield et al., 2011) and any potential anisothermality is not caused by surfaces with heterogeneous thermophysical properties.
315 The daytime brightness temperature differences between the Channel 6 and 7 Diviner data follow a pattern similar to the differences between the Channels 4 and 7 data. During the lunar night, the brightness temperature differences are nearly constant and are typically ~2–5 K; somewhat lower than the noontime measurements. There is no clear signal of residual anisothermality just after sunset.

The model described in Section 2 was applied to each nadir observation for the four ROIs, using the
320 observation average geometric parameters (latitude, longitude, emission angle/azimuth, solar incidence

angle/azimuth, and solar distance), and Clementine-derived local albedo. Each observation was modeled using a RMS roughness of 5–35° at 5° intervals. Similar to the Diviner data, the modeled Diviner brightness temperature differences between separate channels show little variation between the four ROIs. We focus here on the mare ROI for comparison of the model to the measurements, but the other surfaces show similar results.

All modeled surface brightness temperatures show anisothermality and a blue spectral slope that is correlated with solar incidence (Figure 6). The magnitudes of the anisothermality and spectral slope are also highly correlated with the steepness of the surface slopes. Similar to the Diviner measurements, the model predicts little variation (<2K) in anisothermality between 1000H and 1400H for even the roughest surfaces. Unlike the Diviner measurements, modeled brightness temperature spectra and temperature differences are symmetrical about noon, due to the radiative equilibrium nature of the model.

Direct comparison of the model with measurements indicates that no single RMS slope value matches the measurements at all local times. Between 0900H and 1500H, the 20° RMS slope model closely matches the Diviner measurements. However, relative to the measurements, modeled anisothermality increases more rapidly approaching sunrise/sunset. Close to 0600H and 1800H, measurements compare most closely with the 5–10° RMS slope models (Figure 6). This pattern extends to all Diviner wavelengths; modeled anisothermality compares most closely to higher RMS slope distributions closer to noon local time with lower angles of solar incidence (Figure 6).

4.2 EPF observations

4.2.1 Day

The six daytime EPF observations acquired with moderate angles of solar incidence (Table 2; Figure 7) all show a distinct asymmetry in brightness temperature about the nadir observation. In each case, the measurement pointing equatorward has lower brightness temperatures than the equivalent emission

345 angle observation that points poleward. As with the nadir only observations, shorter wavelength EPF observations typically have higher brightness temperatures than longer wavelength observations (Figure 7). There is some variability, especially at higher emission angles due to surface variability in the precise footprint for each separate emission angle observation for each channel.

Superimposed on the general brightness temperature asymmetry, the observations show a decrease in
350 brightness temperature with increasing emission angle at all azimuths about nadir (Figures 7 and 8). Average brightness temperatures decrease by ~4–6K for all channels at 53° emission angles versus nadir. This increases to ~9–11K for Diviner Channels 3–7 at 76° emission angles. There is a more pronounced decrease in brightness temperature of 13 and 25 K for Diviner Channels 8 and 9 respectively.

355 In order to compare the modeled surface roughness properties to the Diviner EPF observations we reduced the EPF data to the difference in brightness temperature between the opposing up- and down-track observations. This maximizes the apparent temperature differences due to roughness effects and minimizes other effects on brightness temperature, such as albedo, thermal inertia, and emissivity (Bandfield and Edwards, 2008). In addition, we averaged the brightness temperature differences in all
360 channels, giving equal weight to each.

As expected, both the model and Diviner measurements show a trend of increasing temperature differences at higher opposing emission angles. Temperature differences reach ~63K for the EPF observation near 98°E, 52°S at opposing 78° up- and down-track emission angle observations. The modeled temperature differences also predict increasing temperature differences for higher RMS
365 surface slope distributions. The six daytime EPF sequences compare most closely with modeled surface slope distributions of ~25–35° (Figure 9).

4.2.2 *Night*

Nighttime EPF measurements show no clear asymmetry in brightness temperature between up- and

down-track observations within 50° of the equator (Figure 10). By contrast, high latitude EPF
370 observations show poleward-facing 76° emission angle observations to be an average of 3–4K higher
than equatorward-facing observations in Diviner Channels 7–9 (Figure 10). Similar to daytime
measurements, higher emission angle nighttime measurements have lower brightness temperatures than
the corresponding nadir observation for a given EPF sequence. For example, average 76° emission
angle observations within 20° of the equator are ~ 5 K lower than the nadir observation in Channels 7
375 and 8 and 8–9K lower in Channel 9.

5. Discussion

5.1 Surface roughness

5.1.1 Measurements

Both Diviner nadir and EPF observations show clear evidence for anisothermality due to surface
380 roughness. Nadir observations have higher brightness temperatures at shorter wavelengths, with
differences that increase in magnitude with increasing angles of solar incidence. Daytime EPF
observations show an increase in brightness temperature across all Diviner channels when viewing
surfaces from the same azimuth as the Sun.

There is no apparent difference in the character of the nadir observations of the four ROIs besides
385 absolute temperatures that are due to albedo variations. Brightness temperature differences between
Diviner channels are similar between the surfaces at all angles of solar incidence. This indicates that
there is little difference in the surface textures at the scale of sensitivity (discussed in Section 5.1.3).
Maria, highlands, dark mantle deposits, and cold spots all appear to have similar slope distributions
regardless of composition and other properties. That the processes responsible for the development of
390 the regolith surface appear independent of surface composition might be expected because it may be
dominated by micrometeorite bombardment and perhaps thermal cycling (e.g., Delbo et al., 2014),
which operates on geologically short timescales.

However, cold spot features show clear differences in thermophysical properties that have been attributed to a thicker low density layer within the upper several centimeters of the lunar regolith (Vasavada et al., 2012; Hayne et al., 2013; Bandfield et al., 2014). We expected this thicker, low density layer to be due to more loosely packed materials. This could result in greater variation in the small-scale topography that would be reflected in a higher surface roughness, but that does not appear to be the case. One possible explanation is that, besides its greater thickness, this low density surface layer does not have different textural properties relative to typical upper lunar regolith. Consequently, textures at the surface may remain unchanged over cold spot surfaces, and the only effect of the thicker low density layer is to lower nighttime surface temperatures. The lack of textural contrast between cold spots and surrounding surfaces is also consistent with visible imaging that also shows no color or intensity contrast under a variety of illumination conditions.

5.1.2 Comparison with models

Our roughness thermal model shows good qualitative agreement with the nadir measurements, and the sign and magnitude of brightness temperatures and brightness temperature differences appear to match the data well. However, close inspection reveals significant differences between the measurements and the modeled data.

Although the lunar surface temperature can be approximated by assuming radiative equilibrium for low angles of solar incidence, there are clear indications near sunrise and sunset where the thermophysical properties of the surface materials influence surface temperatures. Although this effect can be quite subtle in terms of absolute temperature, the relative effects are amplified when comparing brightness temperatures at different wavelengths where sub-K differences can reflect significant differences in surface slope distributions.

Nadir measurements show a distinct asymmetry in brightness temperature differences about noon before 0900H and after 1500H that grows in magnitude approaching sunrise/sunset. This indicates that

our equilibrium model is not appropriate for use at these local times. Between 0900H and 1500H, there is no distinct asymmetry, but brightness temperature differences between Diviner Channels 4 and 7 only show changes of $\sim 3\text{K}$. At these times, the Diviner measurements most closely match the 20° RMS slope model, and the 15° and 25° RMS models show distinctly lower and higher amounts of anisothermality respectively (Figure 6).

Regardless of the temperature difference asymmetry about noon, earlier and later local times more closely match models with lower roughness levels; to the point that the measurements most closely match a 10° RMS slope model near 0600 and 1800H. We do not fully understand why the measurements are in better agreement with smoother modeled surfaces near sunrise and sunset, though we suspect that there are several potential factors; 1) the presence of cast shadows are treated in a simplistic manner in the model and there are potential inaccuracies in the predicted proportion of shadowed surfaces; 2) shadowed surfaces are assumed to be at equilibrium temperature even though the transition from sunlit to shaded conditions can be rapid relative to the rotation of the Moon; 3) illumination conditions in general change more rapidly near sunrise and sunset and again the assumption of radiative equilibrium is likely faulty.

The net effect of factors 2 and 3 described above is to reduce the range of temperatures present within the measurement field of view. Under these conditions, sunlit and shaded surfaces have yet to reach equilibrium and can be cooler and warmer respectively than predicted by the model. The equilibrium model will tend to overestimate anisothermality, resulting in a lower predicted surface roughness. The model is likely more trustworthy between 0900H and 1500H (in agreement with a 20° RMS slope distribution) where cast shadows do not cover a significant proportion of the surface and illumination conditions change slowly.

EPF observations compare most closely with modeled surfaces with $\sim 25\text{--}35^\circ$ RMS slope distributions. There is significant scatter in derived roughness between separate EPF sequences that can be attributed

to variations within the observation footprint between different emission angles. The limited number of daytime EPF sequences with optimal illumination conditions prevents their use much beyond a demonstration of their utility for an initial estimate of surface roughness. Although the level of roughness is somewhat higher than retrieved from the nadir measurements, there is broad agreement
445 between the two types of measurements. A much larger EPF measurement dataset is needed in order to establish trends in apparent roughness with respect to surface units, illumination, and other conditions.

5.1.3 Specific roughness type

We chose to use a Gaussian distribution of slopes here because of its relative simplicity and reasonable fidelity to natural surfaces (e.g., Helfenstein and Shepard, 1999). However, several other surface
450 roughness types have been used with other models. Davidsson et al. (submitted) compared several roughness types and found significant differences in the predicted range of temperatures and resulting modeled radiance. These models included flat surfaces, a series of uniform trenches, spherical segments (e.g., craters embedded within an otherwise flat surface), and a random Gaussian distribution of slopes. An initial comparison of these models with Diviner nadir data showed that only the Gaussian
455 distribution could reasonably match the lunar data (Davidsson et al., submitted).

Regardless, we have also described systematic differences and potential shortcomings between our model and the Diviner measurements. Our goal here is not to uniquely determine the specific roughness distribution. Even though a unique determination of the slope distribution is not probable from these data, the use of a Gaussian slope distribution can serve as a relatively simple baseline against which
460 measurements can be compared. In addition, although there are several specific forms of Gaussian slope distributions (e.g., Hapke, 1985; Spencer, 1990; Helfenstein and Shepard, 1999), there is a significant body of previous work that the results here may be compared against in a relatively direct manner.

5.1.4 *Nighttime measurements*

465 Surface roughness has little apparent effect on nighttime equatorial EPF or nadir measurements. Opposing 73° emission angle observations show differences of less than 0.5K in brightness temperature. The orientation of the EPF observation along the north-south LRO orbit track minimizes variation in observed temperature distributions due to an equatorial sun traveling from east to west. However, nadir oriented measurements would still be expected to show indications of anisothermality
470 regardless of solar azimuth. Despite this, Diviner measurements show little evidence of anisothermality throughout the lunar night, including just after sunset when residual heat from sunlit slopes might be most prominent (Figure 5). Much of the small amount of anisothermality present in the nadir observations (2-5K between Diviner Channels 6 and 7) may be attributed to emissivity variations between spectral bands. High latitude EPF observations do show clear evidence of relatively warm
475 south-facing slopes with $\sim 2\text{--}3\text{K}$ differences in brightness temperature present between opposing 73° emission angle observations (Figure 10).

Even at high latitudes, the relatively modest amount of anisothermality is unlikely to interfere with other effects, such as those due to the presence of high thermal inertia rocks. Typical lunar surfaces are nearly rock-free, but when present, their extremely high temperatures in the lunar night relative to the
480 surrounding regolith overwhelms any residual surface roughness anisothermality signal, including at low rock abundances ($\sim 1\%$).

5.1.5 *Insight from two-dimensional thermal diffusion modeling*

Roughness derived from TIR measurements is sensitive to features with length scales that can remain thermally isolated. For example, although a small pebble may have sunlit and shaded slopes, its high
485 thermal diffusivity will tend to equalize the sunlit and shaded surface temperatures. However, a large boulder will be able to maintain a high temperature contrast throughout the lunar day. By contrast, lunar surface roughness is typically inversely correlated with length scale (Shepard and Campbell, 1998; Lumme et al., 1985; Helfenstein and Shepard, 1999; Campbell et al., 2003). As a result, TIR

roughness measurements characterize the roughness at the smallest scales that can remain thermally
490 isolated.

In this sense, although the lunar highlands may visually appear quite rough and maria appear smooth, meter and larger scale morphologies can have little to no effect on roughness derivations (e.g., Bandfield and Edwards, 2008). There can be exceptions, such as yardangs and dune fields on Mars, where large-scale morphology dominates the roughness measurements (Bandfield and Edwards, 2008;
495 Bandfield, 2009). Most lunar surfaces are generally rock-free, and the surface roughness is dominated by loosely consolidated mounds and clods of lunar regolith. These materials are highly insulating and are capable of maintaining a high temperature contrast between sunlit and shaded slopes.

Buhl et al. (1968) estimated the scale of sensitivity to roughness features from the maximum temperature gradient that could be maintained by the lunar regolith. Using estimates for lunar regolith thermal conductivity, they found the maximum gradient to be 330K/mm. Using updated values for
500 temperature dependent thermal conductivity from Vasavada et al. (2012), we calculated higher values of 500-2200K/mm for material temperatures of 380 and 90 K respectively. It is clear from these estimates that surfaces separated by only a millimeter are capable of maintaining vastly different temperatures.

505 In order to better understand the scale of sensitivity in more detail, we used a two-dimensional thermal diffusion model similar to that described by Williams et al. (2013) and Bandfield and Edwards (2008). This model is intended to provide some insight to the effects of thermal diffusion that are not captured by equilibrium models. Our use of this model is not intended for direct comparison to the Diviner data, which would require many computationally expensive three-dimensional model runs.

510 The model is set at the equator and is composed of a north-south trending series of crests and troughs with an east-west topographic profile that mimics a sine function (Figure 11). The topographic profile was set to 0.001 m, 0.01 m, 0.1 m, and 1 m wavelengths so that sunlit and shaded slopes are separated

by half the wavelength (0.0005, 0.005, 0.05, 0.5 m) and the maximum slope is 32.5° . We used the lunar regolith thermophysical properties described in Vasavada et al. (2012) and Hayne et al. (2013),
515 including temperature and density dependent thermal conductivity and temperature dependent heat capacity. The model assumes that density increases exponentially with depth from 1100 to 1800 kg/m³ with an *e*-folding length scale of 6 cm. Material properties follow the local topography so that the density gradient follows the surface profile.

As expected, when separated by a larger distance, the east- and west-facing slopes show a greater
520 difference in morning and afternoon surface temperatures (Figures 11–13). Surfaces separated by >0.05 m can maintain 160–180K temperature differences near sunrise and sunset (Figure 12). This difference is reduced to ~ 145 and 65 K for the surface slopes separated by 0.005 and 0.0005 m respectively. Temperature differences are relatively small at midday and anisothermality is much reduced compared to conditions with higher angles of solar incidence. Temperatures on illuminated surfaces are not
525 affected by length scale, and are close to the thermal equilibrium approximation.

There is no sharp cutoff scale at which surfaces are or are not thermally isolated, and indeed this scale can change throughout the lunar day as the solar illumination conditions change more or less rapidly. However, it is clear that even at length scales of 0.005 m, surfaces can maintain much of their thermal isolation. At scales of 0.0005 m, this isolation is much reduced, though still considerable for so short a
530 distance. Consequently, we estimate the smallest scale of sensitivity for TIR measurements of the lunar regolith to be larger than 0.0005 m, but less than 0.005 m. At smaller scales, the reduced anisothermality due to thermal diffusion would not be distinguishable from anisothermality due to lower roughness at larger scales.

Unlike the equilibrium model, the two-dimensional model temperatures show a greater range at sunrise
535 than at sunset. This agrees well with the Diviner measurements that show greater anisothermality at early local times (Figures 2 and 5). The diurnal temperature profiles also show a secondary “bump”

immediately preceding local sunrise and after local sunset. This is absent in the equilibrium model, which does not include either reflected sunlight or thermal diffusion from adjacent sunlit surfaces.

These non-equilibrium effects reduce overall surface anisothermality and they are most prominent where conditions are changing most rapidly; mainly near sunrise and sunset. This explains the reduced RMS slopes derived by the equilibrium model from the nadir Diviner measurements (Figure 6). The equilibrium model overestimates anisothermality for a given surface roughness at these local times. The treatment of hard shadows in the equilibrium model introduces cold temperature surfaces instantaneously whereas the more sophisticated model moderates the effects of these surfaces.

At lower angles of solar incidence, the effects of hard shadows are greatly reduced and the equilibrium model more closely matches the results of the two-dimensional diffusion model, such as between 0830 and 1530 H. Under these conditions, the nadir data match a RMS surface slope distribution of $\sim 20^\circ$; somewhat less than the $20\text{--}35^\circ$ RMS slope distribution derived from the Diviner EPF measurements.

At night, residual temperature differences between the east- and west-facing slopes are insignificant, even immediately following sunset. Troughs do remain about 20K warmer than crests throughout the lunar night (Figure 13) due to radiative heating from adjacent surfaces. However, these temperature differences are small when compared to the daytime anisothermality, especially when considering the surface emission in terms of radiance. These small temperature differences are only capable of producing a small range of brightness temperatures between Diviner channels.

5.1.6 Roughness scale and comparison with previous results

Smith (1967) used lunar infrared telescopic measurements to derive RMS slopes of $10\text{--}20^\circ$. The roughness was attributed to large scale surface slopes visible in high resolution telescopic images (estimated to be 9°). The TIR phase behavior was also attributed to cratering of the lunar surface (Sinton, 1962; Buhl et al., 1968; Winter and Krupp, 1971). We find, however, significantly higher RMS slope values that must be attributed to smaller scale surface features that reflect regolith physical

properties. This is in agreement with more recent roughness studies, such as that of Rosenberg et al. (2011), which used LOLA data to derive surface slope distributions at 17m and larger scales. They found median slopes of 2.0–7.6° at 17m length scales, with significant differences between regional terrains. Although the median slope values can be slightly different than the RMS slope values for a given surface, the LOLA slope values are much lower than those reported here. Other meter and larger slope distributions have returned similar low slope values (e.g., Archinal et al., 2011).

The scale of sensitivity and derived RMS slope distributions can be compared to surface slope distributions derived from Apollo Lunar Stereo Closeup Camera images by Helfenstein and Shepard (1999). They derived RMS slope distributions of ~15–29° at length scales of 0.00085m, and ~6–24° at scales of 0.0085m from eleven lunar regolith samples. This is in good agreement with the Diviner results presented here, given the small sample and large range of roughness values.

5.1.7 Regolith surface roughness and textures

Roughness at these small scales is apparent in photographs of undisturbed regolith acquired from the lunar surface (Figure 14; e.g., Carrier and Heiken, 1972). The lunar regolith has a visibly rough, hummocky appearance at millimeter to centimeter scales, and numerous clods and clumps are also visible. Although the presence of clods indicates that the materials are cohesive, they are weak enough to readily disaggregate when disturbed. Astronaut boots, for example, can mold the regolith into a surface that is smooth at millimeter length scales and can maintain vertical surfaces, indicating the cohesive nature of the regolith. Much of the roughness has been attributed to micrometeorite impacts that create what has been described as a “raindrop” appearance. However, the clods and what is described as a weak duricrust (Greenwood et al., 1971; Carrier and Heiken, 1972) indicate that an additional process binds the regolith particles together. These textures are apparent at all of the landing sites, and surface roughness appears uniform at the ROIs investigated here. Although the formation process is not well understood, it appears to be pervasive. The weak cohesiveness of these materials

585 suggests that their individual particles do not have much contact with each other and can maintain a low thermal conductivity and high temperature contrast between sunlit and shaded surfaces, despite their apparently clumpy nature.

5.2 Hemispherical emission

Both daytime and nighttime Diviner EPF observations show a clear decrease in emitted radiance with
590 increasing emission angles (Figures 7 and 8). These effects appear to vary in intensity as a function of wavelength. Given that the Diviner observations do not typically show evidence for significant anisothermality at night based on nadir multispectral measurements (Bandfield et al., 2011), the emission differences cannot be due to the presence of variable temperature surface slopes in the field of view.

595 Fresnel reflection and emission has a strong dependence on the angle of incidence/emission. Although this predicts lower emission with increasing emission angle similar to the Diviner observations described here, there are several inconsistencies with the observations as well. Fresnel reflection for high emissivity materials, such as the lunar regolith (Salisbury et al., 1995; 1997) shows little change in emissivity at emission angles lower than $\sim 60^\circ$. The Diviner EPF observations show a clear decrease in
600 apparent emissivity even in the case of the 53° emission angle observations, and the overall magnitude of the decrease in emissivity is greater than would be predicted by Fresnel emission. Based on both the daytime EPF and nadir observations, the lunar surface is rough. This modifies Fresnel effects on surfaces, increasing the apparent emissivity at greater emission angles and decreasing it at lower emission angles. However, this effect is not significant enough to account for the large changes in
605 emissivity observed with the EPF measurements.

In addition, we also investigated whether multiple scattering of emitted radiance from underlying materials through a thin layer of particulates could have a strong dependence on emission angle. We used a relatively simple two-stream delta-Eddington multiple scattering model (Wiscombe and Warren,

1980) to investigate these potential emission effects. Similar to Fresnel emission, changes in apparent
610 emissivity are most prominent at emission angles greater than $\sim 60^\circ$. In cases where the nadir apparent
emissivity is low, a reduction in emissivity is more prominent in the model at low emission angles.
However, nadir oriented apparent emissivity of the lunar surface is too high for this reduction at low
emission angles to be present based on laboratory measurements of lunar samples and the low spectral
contrast between Diviner spectral channels under isothermal conditions (Salisbury et al., 1997; Figures
615 3–5).

If lateral anisothermality and Fresnel effects can be ruled out, what is the cause of the emission
variations with increasing emission angle? One possible explanation is that the EPF measurements
probe different depths within the surface materials similar to the multiple scattering example described
above. Fine-particulate surface materials in a low pressure or vacuum environment can have severe
620 thermal gradients in the upper few microns (Logan et al., 1973; Hapke, 1996; Henderson and Jakosky,
1997). During the day, solar heating occurs to a depth greater than the emission source, resulting in an
increase in temperature with depth (Hapke, 1996). At night, no solar heating occurs, but there is still a
positive temperature gradient as the immediate surface insulates materials at depth that retain their heat
from the lunar day. Under these circumstances, infrared measurements measure emission integrated
625 over depths that can include significantly different temperatures both day and night. With higher
emission angles, the depth of integration shallows and the surface will appear colder. It is important to
note that this effect may reflect surface textures at the scale that photons interact with the surface
materials. This is controlled by the optical constants of the material for a given wavelength of light. At
TIR wavelengths, this can be highly variable, but can be considerably smaller than the scale of thermal
630 sensitivity discussed in Section 5.1.5.

An additional factor that may be contributing to this effect may be due to the presence of radiatively
insulated concave hollows in the surface. Because the hollows receive both direct sunlight and

downwelling radiance from adjacent surfaces, they can be warmer than topographic peaks both day and night (Figure 13). The concave hollows would be visible from nadir orientations, contributing to the overall measured radiance but hidden from high emission angle observations at all azimuths. Although on a qualitative level, these hypothesis appear viable, both laboratory measurements and detailed modeling would need to be completed to better support (or refute) the mechanisms as an explanation for the Diviner observations.

Regardless of the underlying mechanism, the reduction in emission at high emission angles can have significant effects on both whole disk measurements and the surface radiative balance. To show the magnitude of this effect, we calculated broadband apparent emissivity as a function of emission angle for the daytime and nighttime Diviner EPF observations (Figure 15). Assuming a broadband (Diviner Channels 3–9) nadir emissivity of 0.99, the average daytime apparent emissivity decreases to 0.95, 0.94, 0.93, and 0.92 for the 53, 62, 69, and 76° emission angle observations respectively. Nighttime measurements show apparent emissivity values of 0.92, 0.88, 0.86, 0.82 for the same series of emission angles (using only Diviner Channels 6–9; Channels 3–5 have no detectable signal at cold nighttime temperatures). The apparent emissivity can be approximated by a simple function (Figure 15) and the average hemispherical apparent emissivity can be calculated. Apparent broadband hemispherical emissivity is 0.951 and 0.901 for the average daytime and nighttime EPF measurements respectively. Part of the reason for this day/night difference is the increased proportion of radiance emitted from longer wavelengths (coinciding with the more severe effects present in Diviner data) at colder nighttime temperatures.

The average hemispherical emissivity is significantly lower than is generally assumed for modeling lunar surface temperatures (e.g., Paige et al., 2010; Vasavada et al., 2012; though Hayne et al., 2013 use an emissivity of 0.95). The result of a lower emissivity is a loss of radiative efficiency and higher overall daytime and nighttime surface temperatures. To compensate for the higher hemispherical

emissivity assumed in thermal models, both a lower albedo and higher thermal inertia are required (e.g., Vasavada et al., 2012). Further complicating matters, the apparent hemispherical emissivity changes with surface temperature, and thermal models would need to incorporate this variability to accurately model lunar surface temperatures.

Whole disk measurements are also affected by this effect with an overall apparent emissivity that is significantly lower than that of measurements collected at zenith. This effect is opposite in sign as that of the beaming parameter, resulting in lower brightness temperatures. For example, with a whole disk integrated apparent emissivity of 0.951, the bolometric brightness temperature of a uniform 350K object would be 345.6K. Under the same conditions, except with an apparent emissivity of 0.905 and a 100K object, the brightness temperatures would be 97.5K.

5.3 Implications for measurements of other airless bodies

The Diviner measurements are a unique set of systematic and well-calibrated observations acquired across a wide spectral range. This set of measurements may serve as a starting point for the interpretation of observations from other airless body surfaces, such as asteroids. Clearly, there is a great deal of variety among Solar System objects in terms of thermophysical properties, surface textures, composition, and temperatures. However, the Diviner measurements provide an example of the general behavior of infrared measurements for rough surfaces in a vacuum. These observations can also be used to validate thermal models used to interpret unresolved TIR observations of airless planetary bodies.

The lack of an atmosphere and the fine-particulate nature of many airless body surfaces allows for surfaces to be thermally isolated even at sub-centimeter scales. We have shown here that on the Moon, a surface can have a wide variety of apparent temperatures based on the wavelength or geometry of the measurement. For example, one of the EPF observations that we presented here recorded brightness temperatures that vary by more than 65K based simply on the azimuth of observation.

Thermal infrared measurements of Mercury and asteroids will be acquired by the BepiColumbo, Origins-Spectral Interpretation-Resource Identification-Security-Regolith Explorer (OSIRIS-REx), and Hayabusa-2 spacecraft (Heisinger et al., 2010; Boynton et al., 2012; Yoshikawa et al., 2008). The Diviner measurements may provide a baseline in terms of the expected behavior of these infrared
685 measurements, leading to a more accurate interpretation of surface temperatures and spectral features. This will also provide an initial opportunity to sample the variety that may be present in surface textural and thermophysical properties among airless bodies in the Solar System.

5.4 Implications for short wavelength observations

Near infrared measurements have been used to derive surface temperatures and thermophysical
690 properties for the Moon and a variety of Solar System bodies (Clark et al., 2011; Groussin et al., 2013; Keihm et al., 2013; Capria et al., 2014; Audouard et al., 2014). In addition, the thermal contribution to the measured radiance at short wavelengths must be accounted for in order to properly interpret spectral features (e.g., Pieters et al., 2009). Surface roughness and the resulting anisothermality will have significant effects on these measurements and must be accounted for in order to accurately
695 interpret shorter wavelength datasets.

With a surface of mixed temperatures, longer wavelength observations have brightness temperatures that approach the areal weighted average temperature. Conversely, shorter wavelength observations have brightness temperatures that approach the highest temperature within the field of view, no matter how small the proportion of the area at that temperature. Use of near-infrared measurements for the
700 derivation of surface temperatures has similar properties as the shorter wavelength Diviner measurements, and the measured brightness temperatures can often be much higher than the average surface temperature in the field of view. In addition, the brightness temperature will not be constant with respect to wavelength even within limited spectral ranges. The severe effects of surface roughness on near-infrared observations warrants a separate investigation to more fully explore and quantify the

705 magnitude of the roughness effects and the implications for thermophysical and spectral interpretations.

6. Conclusions

Diviner TIR measurements show that the Moon can be highly anisothermal due to surface roughness.

We were able to detect and quantify this roughness using both multispectral nadir and multiple

emission angle data combined with a relatively simple equilibrium thermal roughness model. An

710 assessment of four lunar surface units using nadir data shows no significant differences in surface

roughness, and can be fit well assuming a RMS slope distribution of $\sim 20^\circ$. Multiple emission angle

observations from several sites are most closely modeled using higher RMS slope distributions of ~ 20 –

35°. The similarity in surface roughness among these geologically distinct units implies that the impact

gardening process responsible for generating the lunar small-scale roughness occurs on a rapid

715 timescale, and is independent of geologic unit type.

Our simple model appears to work well for low angles of solar incidence, where radiative equilibrium

is closely approximated. However, thermal diffusion modeling shows that the simple model is less

accurate under more rapidly changing radiative conditions with a greater proportion of hard shadows.

The diffusion modeling also indicates that TIR measurements are sensitive to surface roughness

720 features with length scales greater than 0.0005 to 0.005 m. This is similar to the size of surface

structures that develop in the lunar regolith.

We have also more fully characterized the lunar surface radiative environment. Lunar emission shows a

significant decrease with increasing emission angle at all local times. As a result, surface radiative

efficiency is lower than would otherwise be assumed by extrapolating from nadir-oriented

725 measurements. This effect should be incorporated in lunar thermal models and will also counter-

balance the effects of surface roughness beaming from whole-disk measurements.

A detailed characterization of the wavelength and phase angle dependent radiative behavior of the lunar

surface can be used to better understand other datasets, such as near-infrared measurements that have

thermal contributions that are particularly sensitive to surface roughness. In addition, the work
730 presented here may serve as a basis for comparison with similar measurements of other airless bodies,
and may be used as an initial template for the interpretation of TIR measurements acquired under a
variety of geometric conditions.

Acknowledgments

We would like to thank the LRO, LROC, LOLA, and Diviner operations teams for the collection of
735 high quality datasets used in this work. Ian Thomas provided validation for the initial Diviner multiple
emission angle observations. Björn Davidsson and an anonymous reviewer provided kind and
constructive comments that improved both the clarity and content of the manuscript. Support for this
work was provided by the Lunar Reconnaissance Orbiter program and NASA Planetary Geology and
Geophysics program grant NNX12AO46G. This work also benefited from discussions at meetings
740 supported by the International Space Science Institute (ISSI). Part of this work was carried out at the
Jet Propulsion Laboratory, under contract with the National Aeronautics and Space Administration.

References

- Archinal, B. A., and 14 colleagues (2011) Progress on High Resolution Mapping of the Lunar South Pole-Aitken Basin Interior. *Lunar Planet. Sci. Conf.*, 42, 2316.
- 745 Audouard, J., F. Poulet, M. Vincendon, J.-P. Bibring, F. Forget, Y. Langevin, and B. Gondet (2014) Mars surface thermal inertia and heterogeneities from OMEGA/MEX. *Icarus*, 233, 194-213 10.1016/j.icarus.2014.01.045.
- Bandfield, J. L. (2009) Effects of surface roughness and graybody emissivity on martian thermal infrared spectra. *Icarus*, 202, 414-428, 10.1016/j.icarus.2009.03.031.
- 750 Bandfield, J. L. and C. S. Edwards (2008) Derivation of martian surface slope characteristics from directional thermal infrared radiometry. *Icarus*, 193, 139-157, 10.1016/j.icarus.2007.08.028.
- Bandfield, J. L. and M. D. Smith (2003) Multiple emission angle surface-atmosphere separations of thermal emission spectrometer data. *Icarus*, 161, 47-65 10.1016/S0019-1035(02)00025-8.
- 755 Bandfield, J. L., E. Song, P. O. Hayne, B. D. Brand, R. R. Ghent, A. R. Vasavada, and D. A. Paige (2014) Lunar cold spots: Granular flow features and extensive insulating materials surrounding young craters. *Icarus*, 231, 221-231 10.1016/j.icarus.2013.12.017.
- Bandfield, J. L., et al. Lunar surface rock abundance and regolith fines temperatures derived from LRO Diviner Radiometer data. *J. Geophys. Res.*, 116, 010.1029/2011JE003866 (2011).
- 760 Boynton, W. V., and 15 colleagues (2012) The OSIRIS-REx mission to RQ36: nature of the remote sensing observations. European Planetary Science Congress 2012, 875.
- Buhl, D., W. J. Welch, and D. G. Rea (1968) Reradiation and Thermal Emission from Illuminated Craters on the Lunar Surface. *J. Geophys. Res.*, 73, 5281 10.1029/JB073i016p05281.
- 765 Campbell, B. A., L. M. Carter, D. B. Campbell, M. Nolan, J. Chandler, R. R. Ghent, B. Ray Hawke, R. F. Anderson, and K. Wells (2010) Earth-based 12.6-cm wavelength radar mapping of the Moon: New views of impact melt distribution and mare physical properties. *Icarus*, 208, 565-573 10.1016/j.icarus.2010.03.011.
- Campbell, B. A., B. R. Hawke, and D. B. Campbell (2009) Surface morphology of domes in the Marius Hills and Mons Rümker regions of the Moon from Earth-based radar data. *J. Geophys. Res.*, 114, 100110.1029/2008JE003253.
- 770 Campbell, B.A., Ghent, R.R., Shepard, M.K., 2003. Limits on inference of Mars small-scale topography from MOLA data. *Geophys. Res. Lett.*, 30, 10.1029/2002GL016550.
- Capria, M. T., and 16 colleagues (2014) Vesta surface thermal properties map. *Geophys. Res. Lett.*, 41, 1438-1443 10.1002/2013GL059026.
- 775 Carrier, W. D. III, and G. Heiken (1972) *Lunar Surface Closeup Stereoscopic Photography at Fra Mauro (Apollo 14 Site)*. NASA Technical Memorandum X-58072, 53 pp.
- Carter, L. M., C. D. Neish, D. B. J. Bussey, P. D. Spudis, G. W. Patterson, J. T. Cahill, and R. K. Raney (2012) Initial observations of lunar impact melts and ejecta flows with the Mini-RF radar. *J. Geophys. Res.*, 117, 010.1029/2011JE003911.
- 780 Clark, R. N., C. M. Pieters, R. O. Green, J. W. Boardman, and N. E. Petro (2011) Thermal removal from near-infrared imaging spectroscopy data of the Moon. *J. Geophys. Res.*, 116, 010.1029/2010JE003751.

- Davidsson, B. J. R., and 12 colleagues (2013) Thermal inertia and surface roughness of Comet 9P/Tempel 1. *Icarus*, 224, 154-171 10.1016/j.icarus.2013.02.008.
- 785 Davidsson, B. J. R., P. J. Guitiérrez, and H. Rickman (2009) Physical properties of morphological units on Comet 9P/Tempel 1 derived from near-IR Deep Impact spectra. *Icarus*, 201, 335-357 10.1016/j.icarus.2008.12.039.
- Davidsson, B. J. R., H. Rickman, J. L. Bandfield, O. Groussin, P. J. Guitiérrez, M. Wilska, M.T. Capria, J. P. Emery, A. Maturilli, T.G. Mueller (2014) Interpretation of thermal emission. I. The effect of roughness for spatially resolved atmosphereless bodies. *Icarus*, in review.
- 790 Delbo, M., G. Libourel, J. Wilkerson, N. Murdoch, P. Michel, K. T. Ramesh, C. Ganino, C. Verati, and S. Marchi (2014) Thermal fatigue as the origin of regolith on small asteroids. *Nature*, 508, 233-236 10.1038/nature13153.
- Gaddis, L. R., C. M. Pieters, and B. R. Hawke (1985) Remote sensing of lunar pyroclastic mantling deposits. *Icarus*, 61, 461-489 10.1016/0019-1035(85)90136-8.
- 795 Ghent, R. R., P. O. Hayne, J. L. Bandfield, B. A. Campbell, L. M. Carter, C. Allen, and D. A. Paige (2012) Constraints on the recent rate of lunar regolith accumulation from Diviner observations, *AGU Fall Meeting Abs.*, 2012AGUFM.P42A07H.
- Ghent, R. R., D. W. Leverington, B. A. Campbell, B. R. Hawke, and D. B. Campbell Earth-based observations of radar-dark crater haloes on the Moon: Implications for regolith properties. *J. Geophys. Res.*, 110, 10.1029/2004JE002366 (2005).
- 800 Goguen, J. D., T. C. Stone, H. H. Kieffer, and B. J. Buratti (2010) A new look at photometry of the Moon. *Icarus*, 208, 548-557 10.1016/j.icarus.2010.03.025.
- Gold, T. (1970) Apollo 11 and 12 Close-Up Photography. *Icarus*, 12, 360-375 10.1016/0019-1035(70)90005-9.
- 805 Greenhagen, B. T., and 12 colleagues (2010) Global Silicate Mineralogy of the Moon from the Diviner Lunar Radiometer. *Science*, 329, 150710.1126/science.1192196.
- Greenwood, W. R., Jones, R. L., Heiken, G. H., Bender, M. J., and Hill, R. O. (1971) *Lunar-Surface Closeup Stereoscopic Photography on the Sea of Tranquility (Apollo 11 Landing Site)*. NASA Technical Memorandum X-58077, 23 pp.
- 810 Groussin, O., and 15 colleagues (2013) The temperature, thermal inertia, roughness and color of the nuclei of Comets 103P/Hartley 2 and 9P/Tempel 1. *Icarus*, 222, 580-594 10.1016/j.icarus.2012.10.003.
- Hagfors, T. (1967) A study of the depolarization of lunar radar echoes. *Radio Science*, 2, 445.
- 815 Hapke, B. (1984) Bidirectional reflectance spectroscopy. III - Correction for macroscopic roughness. *Icarus*, 59, 41-59 10.1016/0019-1035(84)90054-X.
- Hapke, B. (1996) Applications of an energy transfer model to three problems in planetary regoliths: The solid-state greenhouse, thermal beaming, and emittance spectra. *J. Geophys. Res.*, 101, 16833-16840 10.1029/96JE00918.
- 820 Haruyama, J., M. Ohtake, T. Matsunaga, and Lism Working Group (2006) Global High-Resolution Stereo Mapping of the Moon with the Selene Terrain Camera. *Advances in Geosciences, Volume 3: Planetary Science*, 3, 101.
- Hayne, P. O., R. Ghent, J. L. Bandfield, A. R. Vasavada, M. A. Siegler, B. T. Greenhagen, J.-P. Williams, and D. A. Paige (2013) Formation and Evolution of the Moon's Upper Regolith:

- Constraints from Diviner Thermal Measurements. *Lunar Planet. Sci. Conf.*, 44, 3003.
- 825 Helfenstein, P. and M. K. Shepard (1999) Submillimeter-Scale Topography of the Lunar Regolith. *Icarus*, 141, 107-131, 10.1006/icar.1999.6160.
- Helfenstein, P. and J. Veverka (1987) Photometric properties of lunar terrains derived from Hapke's equation. *Icarus*, 72, 342-357 10.1016/0019-1035(87)90179-5.
- 830 Henderson, B. G. and B. M. Jakosky (1997) Near-surface thermal gradients and mid-IR emission spectra: A new model including scattering and application to real data. *J. Geophys. Res.*, 102, 6567-6580 10.1029/96JE03781.
- Hiesinger, H., J. Helbert, and Mertis Co-I Team (2010) The Mercury Radiometer and Thermal Infrared Spectrometer (MERTIS) for the BepiColombo mission. *Planet. Space Sci.*, 58, 144-165 10.1016/j.pss.2008.09.019.
- 835 Isbell, C. E., E. M. Eliason, K. C. Adams, T. L. Becker, A. L. Bennett, E. M. Lee, A. S. McEwen, M. S. Robinson, J. R. Shinaman, and L. A. Weller (1999) Clementine: A Multi-Spectral Digital Image Model Archive of the Moon. *Lunar Planet. Sci. Conf.*, 30, 1812.
- Jakosky, B. M., G. W. Finiol, and B. G. Henderson (1990) Directional variations in thermal emission from geologic surfaces. *Geophys. Res. Lett.*, 17, 985-988 10.1029/GL017i007p00985.
- 840 Jamsa, S., J. I. Peltoniemi, and K. Lumme (1993) Thermal emission from a rough surface: ray optics approach. *Astron. Astrophys.*, 271, 319.
- Johnson, P. E., K. J. Vogler, and J. P. Gardner (1993) The effect of surface roughness on lunar thermal emission spectra. *J. Geophys. Res.*, 98, 20825 10.1029/93JE02275.
- 845 Keihm, S. J., and M. G. Langseth Jr. Surface brightness temperatures at the Apollo 17 heat flow site: Thermal conductivity of the upper 15 cm of regolith. (1973) *Lunar Planet. Sci. Conf.*, 4.
- Keihm, S., L. Kamp, S. Gulkis, M. Hofstadter, S. Lee, M. Janssen, and M. Choukroun (2013) Reconciling main belt asteroid spectral flux density measurements with a self-consistent thermophysical model. *Icarus*, 226, 1086-1102 10.1016/j.icarus.2013.07.005.
- 850 Kreslavsky, M. A., J. W. Head, G. A. Neumann, M. A. Rosenburg, O. Aharonson, D. E. Smith, and M. T. Zuber (2013) Lunar topographic roughness maps from Lunar Orbiter Laser Altimeter (LOLA) data: Scale dependence and correlation with geologic features and units. *Icarus*, 226, 52-66 10.1016/j.icarus.2013.04.027.
- Lagerros, J. S. V. (1998) Thermal physics of asteroids. IV. Thermal infrared beaming. *Astron. Astrophys.*, 332, 1123-1132.
- 855 Logan, L. M., G. R. Hunt, J. W. Salisbury, and S. R. Balsamo (1973) Compositional Implications of Christiansen Frequency Maximums for Infrared Remote Sensing Applications. *J. Geophys. Res.*, 78, 4983-5003 10.1029/JB078i023p04983.
- Lumme, K., H. Karttunen, and W. M. Irvine (1985) Roughness of the lunar soil. *Earth Moon and Planets*, 33, 19-29 10.1007/BF00054707.
- 860 Mahanti, P., M. S. Robinson, and R. Stelling (2014) How Deep and Steep are Small Lunar Craters? - New Insights from LROC NAC DEMs. *Lunar Planet. Sci. Conf.*, 45, 1584.
- Paige, D. A., et al. The Lunar Reconnaissance Orbiter Diviner Lunar Radiometer Experiment. *Space Sci. Rev.*, 150, 125-160 10.1007/s11214-009-9529-2 (2010).
- 865 Paige, D. A., and 26 colleagues (2010) Diviner Lunar Radiometer Observations of Cold Traps in the Moon's South Polar Region. *Science*, 330, 479 10.1126/science.1187726.

- Pettit, E. and S. B. Nicholson (1930) Lunar radiation and temperatures. *The Astrophysical Journal*, 71, 102-135, 10.1086/143236.
- Pieters, C. M., and 28 colleagues (2009) Character and Spatial Distribution of OH/H₂O on the Surface of the Moon Seen by M3 on Chandrayaan-1. *Science*, 326, 56810.1126/science.1178658.
- 870 Robinson, M. S., and 22 colleagues (2010) Lunar Reconnaissance Orbiter Camera (LROC) Instrument Overview. *Space Science Rev.*, 150, 81-124 10.1007/s11214-010-9634-2.
- Rosenburg, M. A., O. Aharonson, J. W. Head, M. A. Kreslavsky, E. Mazarico, G. A. Neumann, D. E. Smith, M. H. Torrence, and M. T. Zuber (2011) Global surface slopes and roughness of the Moon from the Lunar Orbiter Laser Altimeter. *J. Geophys. Res.*, 116, 200110.1029/2010JE003716.
- 875 Rozitis, B. and Green, S. F. (2012) The influence of rough surface thermal-infrared beaming on the Yarkovsky and YORP effects. *Royal Astronom. Soc.*, 423, 367–388.
- Salisbury, J.W., D.G. Murcray, W.J. Williams, and R.D. Blatherwick (1995) Thermal infrared spectra of the Moon. *Icarus*, 115, 181-190.
- Salisbury, J. W., A. Basu, and E. M. Fischer (1997) Thermal Infrared Spectra of Lunar Soils. *Icarus*,
880 130, 125-139 10.1006/icar.1997.5809.
- Shepard, M. K. and P. Helfenstein (2007) A test of the Hapke photometric model. *J. Geophys. Res.*, 112, 300110.1029/2005JE002625.
- Shepard, M. K., Campbell, B. A. (1998) Shadows on a planetary surface and implications for photometric roughness. *Icarus*, 134, 279–291.
- 885 Shepard, M. K., R. A. Brackett, and R. E. Arvidson (1995) Self-affine (fractal) topography: Surface parameterization and radar scattering. *J. Geophys. Res.*, 100, 11709-11718 10.1029/95JE00664.
- Shkuratov, Y. G., D. G. Stankevich, D. V. Petrov, P. C. Pinet, A. M. Cord, Y. H. Daydou, and S. D. Chevrel (2005) Interpreting photometry of regolith-like surfaces with different topographies: shadowing and multiple scattering. *Icarus*, 173, 3-15 10.1016/j.icarus.2003.12.017.
- 890 Sinton, W.M. (1962) Temperatures on the lunar surface. In: Kopal, Z. (Ed.), *Physics and Astronomy of the Moon*. Academic Press, New York, pp. 407–428.
- Smith, B. G. (1967) Lunar Surface Roughness: Shadowing and Thermal Emission. *Journal of Geophysical Research*, 72, 4059-4067.
- Smith, D. E., and 30 colleagues (2010) The Lunar Orbiter Laser Altimeter Investigation on the Lunar
895 Reconnaissance Orbiter Mission. *Space Sci. Rev.*, 150, 209–241, 10.1007/s11214-009-9512-y.
- Spencer, J. R. (1990) A rough-surface thermophysical model for airless planets. *Icarus*, 83, 27-38 10.1016/0019-1035(90)90004-S.
- Thompson, T. W., H. Masursky, R. W. Shorthill, G. L. Tyler, and S. H. Zisk (1974) A comparison of infrared, radar, and geologic mapping of lunar craters. *Moon*, 10, 87-117 10.1007/BF00562019.
- 900 Thompson, T. W., B. A. Campbell, R. R. Ghent, B. R. Hawke, and D. W. Leverington (2006) Radar probing of planetary regoliths: An example from the northern rim of Imbrium basin. *J. Geophys. Res.*, 111, 610.1029/2005JE002566.
- Vasavada, A. R., et al. Lunar equatorial surface temperatures and regolith properties from the Diviner Lunar Radiometer Experiment. *J. Geophys. Res.*, 117, 010.1029/2011JE003987 (2012).
- 905 Williams, J., D. A. Paige, P. O. Hayne, A. R. Vasavada, and J. L. Bandfield (2013) Modeling Anisothermality in LRO Diviner Observations to Assess Surface Roughness and Rock Abundance.

AGU Fall Meeting Abstracts, 2021.

- Winter, D. F. (1970) The infrared moon: data, interpretation, and implications. *Radio Science*, 5, 229-240, 10.1029/RS005i002p00229.
- 910 Winter, D. F. and J. A. Krupp (1971) Directional characteristics of infrared emission from the moon. *Moon*, 2, 279-292 10.1007/BF00561881.
- Wiscombe, W. J. and S. G. Warren (1980) A Model for the Spectral Albedo of Snow. I: Pure Snow. *J. Atm. Sci.*, 37, 2712-2733.
- 915 Yoshikawa, M., H. Yano, J. Kawaguchi, Hayabusa-2 Pre-Project Team, and Small Body Exploration Wg (2008) Japan's Future Plans for Missions to Primitive Bodies: Hayabusa-2, Hayabusa-Mk2, and Marco Polo. *Lunar Planet. Sci. Conf.*, 39, 1747.

Tables

Table 1. Regions of interest for nadir-oriented Diviner measurements.

Region of Interest	Longitude	Latitude	Orbit Tracks
Mare	304.65–307.86°E	-0.13–0.16°N	721
Highlands	210.56–213.87	-0.14–0.13	733
Dark Mantle	350.93–352.41	5.24–5.51	166
Cold Spot	151.18–152.33	-3.74–3.55	122

Table 2. Diviner Emission phase function observations used for this study. The orbits marked with an asterisk were used for roughness derivations. All orbits were used for characterization of apparent emissivity as a function of emission angle.

LRO Orbit	Longitude	Latitude	Local Time	Solar Incidence	Solar Azimuth	Temperature
Day						
5497	-96.3°E	-9.4°N	13.8	27°	75°	373K
5497*	-96.0	-25.7	13.8	35	51	365
5498*	-97.8	22.2	13.7	34	130	360
5498	-97.6	8.6	13.7	28	110	377
6005*	98.2	-52.3	11.2	52	344	340
6006*	95.6	22.0	11.1	27	212	379
6006	95.8	8.4	11.1	17	235	387
6352	97.9	-9.7	9.3	42	279	361
6352*	98.2	-25.8	9.3	46	296	356
6353*	96.3	21.8	9.2	47	246	352
6353	96.5	8.2	9.2	42	259	357
Night						
4450	-92.2	-9.3	19.1			114
4450	-92.0	-25.7	19.1			111
4451	-93.7	22.3	19.0			114
4800	85.9	4.6	5.3			94
4800	86.0	18.3	5.3			93
4800	86.3	34.8	5.3			91
4800	86.7	48.5	5.4			86
5150	83.6	12.9	3.5			95
5150	83.8	26.6	3.6			95
5150	84.7	57.6	3.6			85
5498	83.5	29.2	1.8			96
5498	83.8	42.9	1.8			91
5498	84.5	59.3	1.9			85
6006	-83.3	11.2	23.1			100
6006	-80.7	70.3	23.3			81
6352	-83.4	-30.6	21.2			102
6352	-83.1	-16.7	21.2			104
6352/6353	-82.8	0.0	21.3			104
6701	-84.5	-12.9	19.4			110
6701	-84.3	1.0	19.4			112
7397	98.7	-68.4	3.9			77
7398	94.1	22.1	3.6			93
7398	94.4	8.4	3.6			95

Figure Captions

- 925 **Figure 1.** Clementine global 750nm mosaic. Red and blue symbols show the locations of daytime and nighttime emission phase function observations respectively. Green areas show the locations of the nadir-oriented measurements used in this study.
- Figure 2.** Diviner Channel 4 (8.2 μm) minus Channel 7 (25–41 μm) brightness temperature differences for nadir-oriented measurements for each of the 4 regions of interest used in this study. Scatter is higher for the highlands and cold spot locations because of topographic variability within the measurement areas.
- 930 **Figure 3.** Diviner mare region of interest spectra from near sunrise to noon local times. The blue spectral slope increases with increasing solar incidence and greater anisothermality. All spectra are shown in brightness temperature relative to Diviner Channel 4 (8.2 μm).
- Figure 4.** Diviner Channel 4 (8.2 μm ; red) and Channel 7 (25–41 μm ; blue) brightness temperatures for each of the 4 regions of interest showing diurnal temperature variations and the increased separation of brightness temperatures between the two channels near sunrise and sunset. Channel 4 temperatures are 935 unreliable below $\sim 150\text{K}$ and are not valid at night.
- Figure 5.** Diviner Channel 6 (13–23 μm) minus Channel 7 (25–41 μm) brightness temperature differences for nadir-oriented measurements for the mare region of interest used in this study. Anisothermality is restricted to high angles of solar incidence and is not significant during the night or 940 near equatorial noon.
- Figure 6.** Diviner Channel 4 (8.2 μm) minus Channel 7 (25–41 μm) brightness temperature differences for nadir-oriented measurements for the mare region of interest used in this study (black triangles). Modeled Diviner brightness temperature differences for RMS slopes of 10, 15, 20, and 25° are also shown. The bottom plot shows a subset of the data designated by the rectangle in the top plot.
- 945 **Figure 7.** Diviner daytime emission phase function measurements for Channels 4, 6, and 9 (8.2, 13–23,

and 100–300 μm). Each observation set (Table 2) includes measurements made from the north (negative emission angles), nadir, and from the south (positive emission angles). Inc and Az are the solar incidence and azimuth (degrees clockwise from north) respectively for each observation set.

Figure 8. Decline in brightness temperature as a function of emission angle relative to the nadir-oriented observation. Data are taken from the average of all daytime emission phase function observations listed in Table 2. Diviner Channels 3 and 5 are not shown for clarity, but follow a pattern similar to that of Channel 4. Observations include averages of both poleward- and equatorward-facing observations (distinguished by positive and negative emission angles in Figure 7), which largely cancels out roughness effects that are azimuth dependent.

Figure 9. Comparison of Diviner daytime emission phase function observations (red symbols and lines) to RMS roughness models with mean slopes of 5–45° (black lines). Data and models are an average of all Diviner spectral channels. The brightness temperatures in the plots represent the difference between opposing north- and south-facing emission angle observations. Inc and Az are the solar incidence and azimuth (degrees clockwise from north) respectively for each observation set.

Figure 10. Average brightness temperatures for nighttime emission phase function observations at latitudes poleward of 50° latitude (top) and equatorward of 50° (bottom). Negative emission angles correspond to viewing angles from the equatorward direction and positive emission angles correspond to viewing angles from the poleward direction.

Figure 11. 2-dimensional temperature model results for a local time of 0800H with the sun in the east at an incidence of 60°. Each image shows an east-west trending cross section for the 4 separate length scales that were investigated. Specific surfaces discussed in Figures 12 and 13 are labeled in the top cross section.

Figure 12. Temperature differences between the east- and west- facing slopes (denoted in Figure 11) for the 4 length scales as a function of local time. Smaller length scales are unable to remain as

970 thermally isolated as the larger scale features.

Figure 13. Surface temperatures for the east- and west-facing slopes, crest, and trough surfaces denoted in Figure 11. Two length scales are shown; 5cm, where the four surfaces remain thermally isolated, and 0.5mm, where the thermal isolation is significantly reduced.

Figure 14. Apollo image AS15-82-11155 showing several lunar regolith textures; undisturbed regolith,
975 a rake sample collection site indicated by the parallel linear ridges, and compressed and smoothed regolith that is present within the astronaut boot prints.

Figure 15. Diviner broadband apparent emissivity as a function of emission angle (red crosses) for daytime (top) and nighttime (bottom) emission phase function observations. Nadir emissivity is assumed to be 0.99. The equations (black lines) are fits to the data used to calculate hemispherical
980 emissivity discussed in the text.

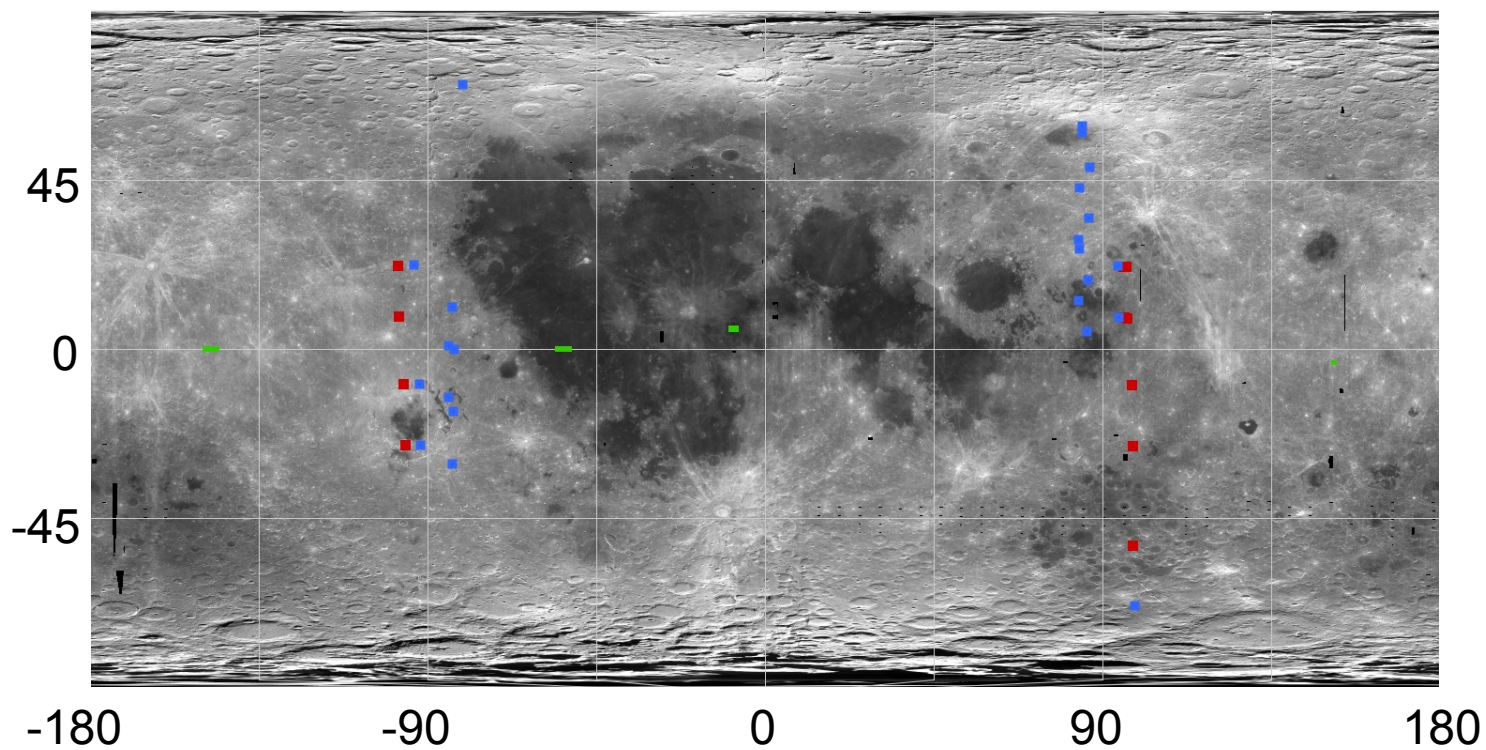


Figure 1. Clementine global 750nm mosaic. Red and blue symbols show the locations of daytime and nighttime emission phase function observations respectively. Green areas show the locations of the nadir-oriented measurements used in this study.

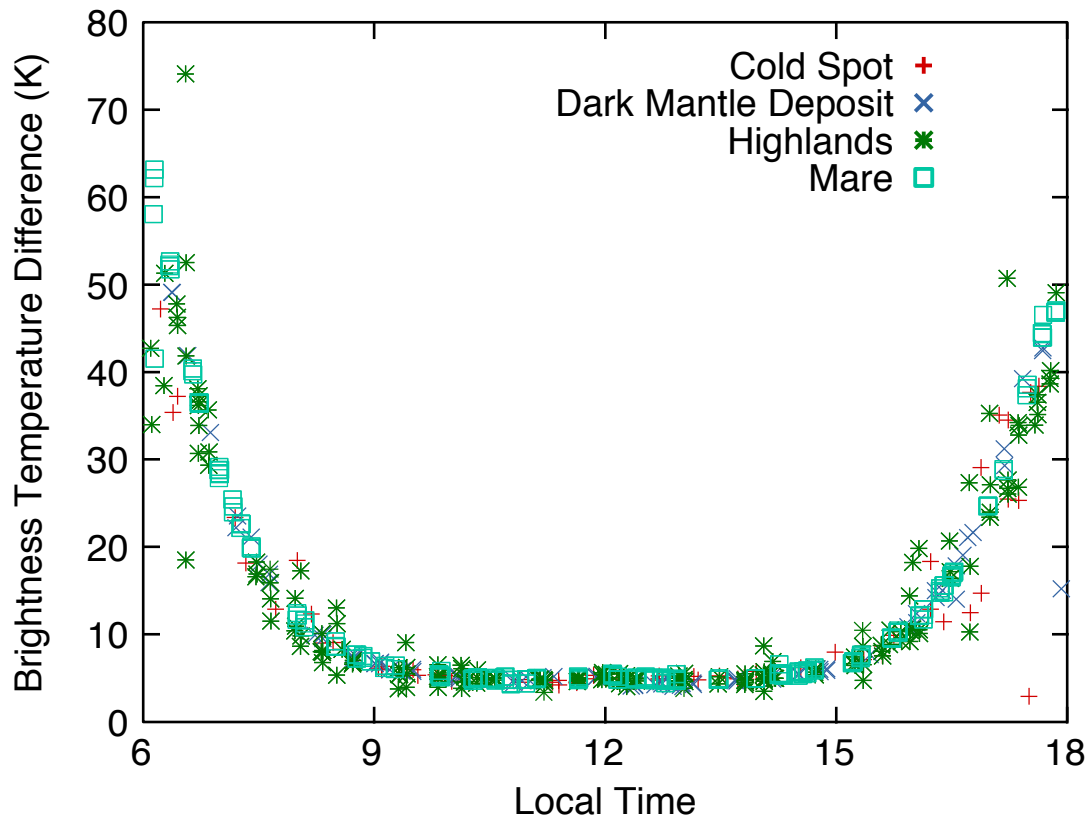


Figure 2. Diviner Channel 4 (8.2 μm) minus Channel 7 (25–41 μm) brightness temperature differences for nadir-oriented measurements for each of the 4 regions of interest used in this study. Scatter is higher for the highlands and cold spot locations because of topographic variability within the measurement areas.

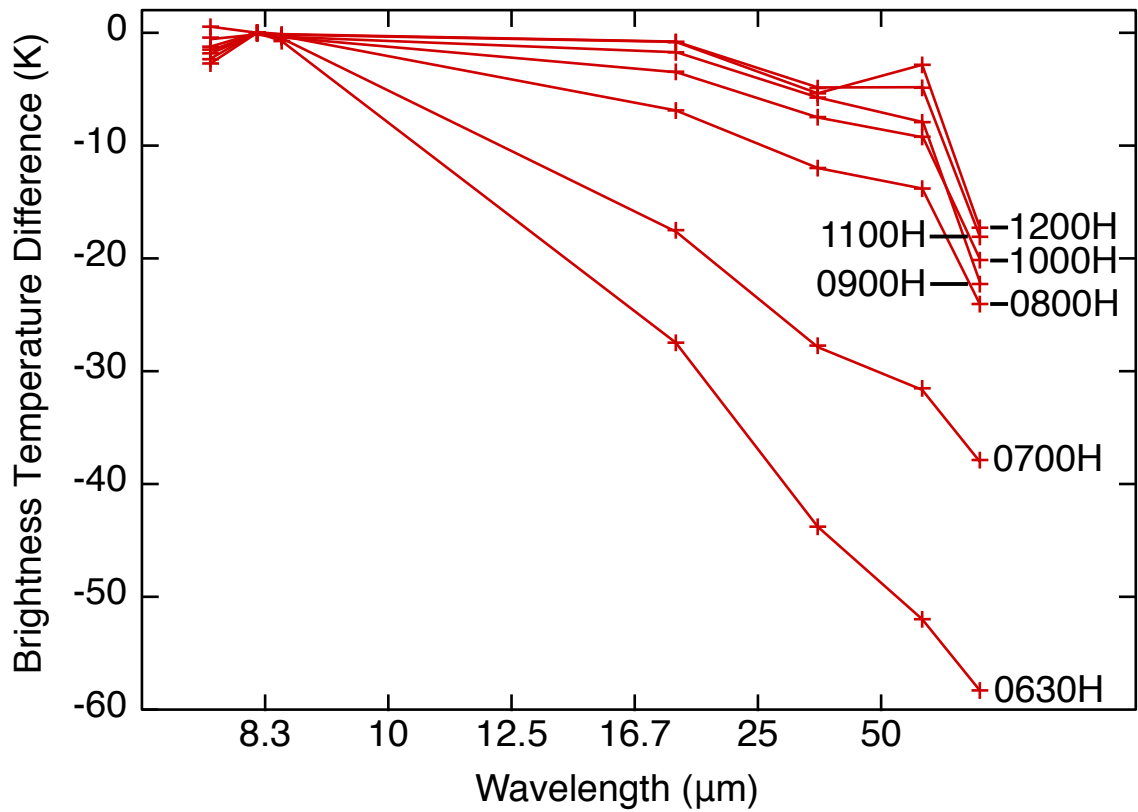


Figure 3. Diviner mare region of interest spectra from near sunrise to noon local times. The blue spectral slope increases with increasing solar incidence and greater anisothermality. All spectra are shown in brightness temperature relative to Diviner Channel 4 (8.2 μm).

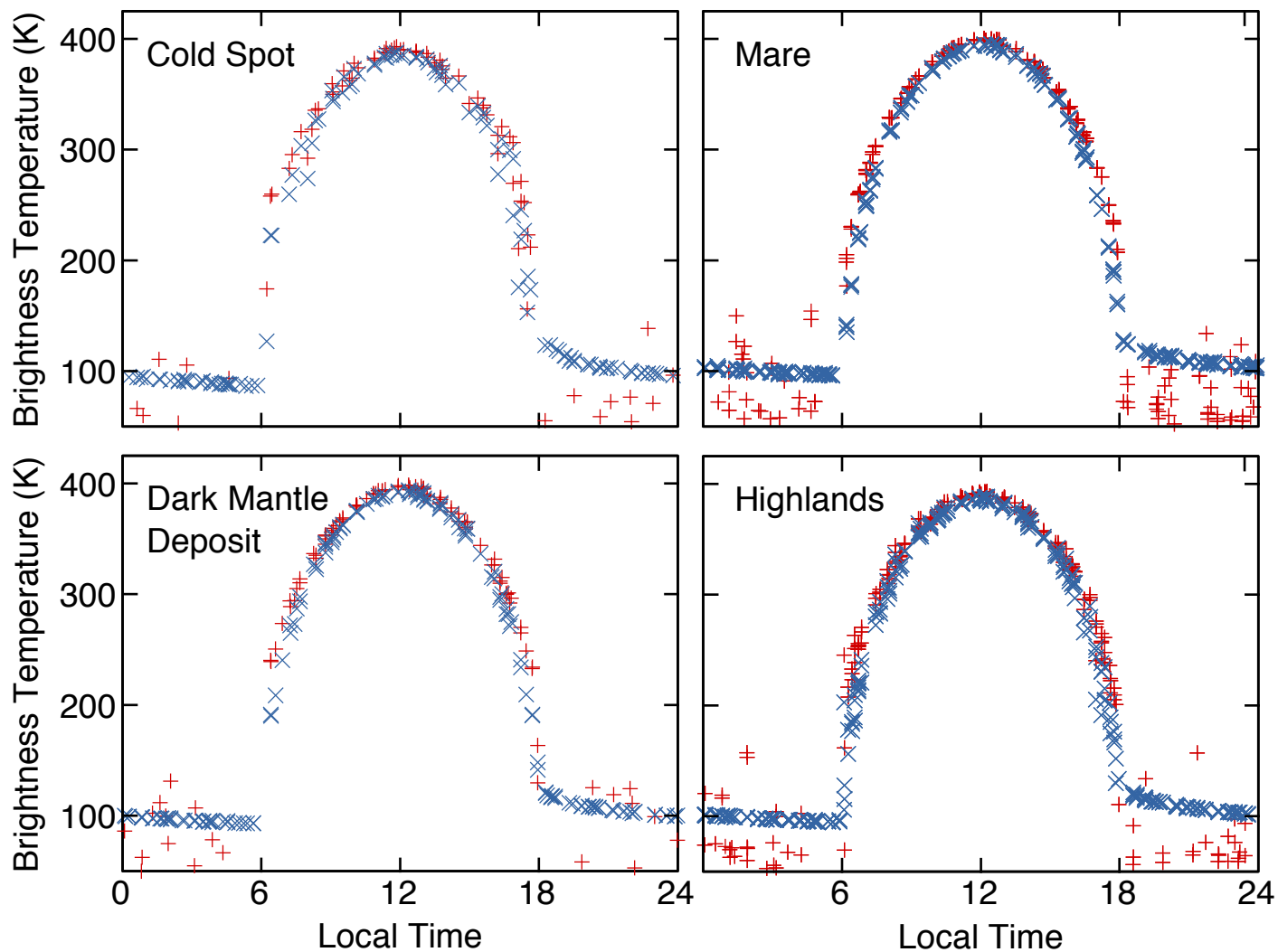


Figure 4. Diviner Channel 4 (8.2 μm ; red) and Channel 7 (25–41 μm ; blue) brightness temperatures for each of the 4 regions of interest showing diurnal temperature variations and the increased separation of brightness temperatures between the two channels near sunrise and sunset. Channel 4 temperatures are unreliable below $\sim 150\text{K}$ and are not valid at night.

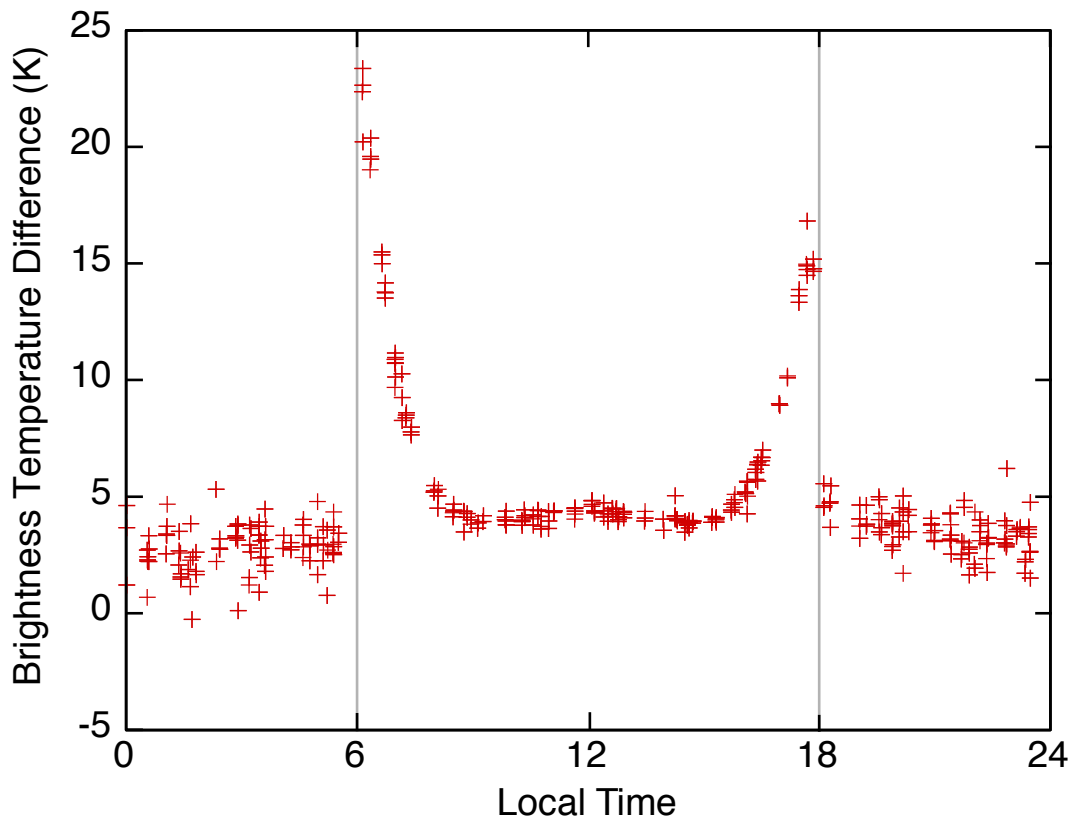


Figure 5. Diviner Channel 6 (13–23 μm) minus Channel 7 (25–41 μm) brightness temperature differences for nadir-oriented measurements for the mare region of interest used in this study. Anisothermality is restricted to high angles of solar incidence and is not significant during the night or near equatorial noon.

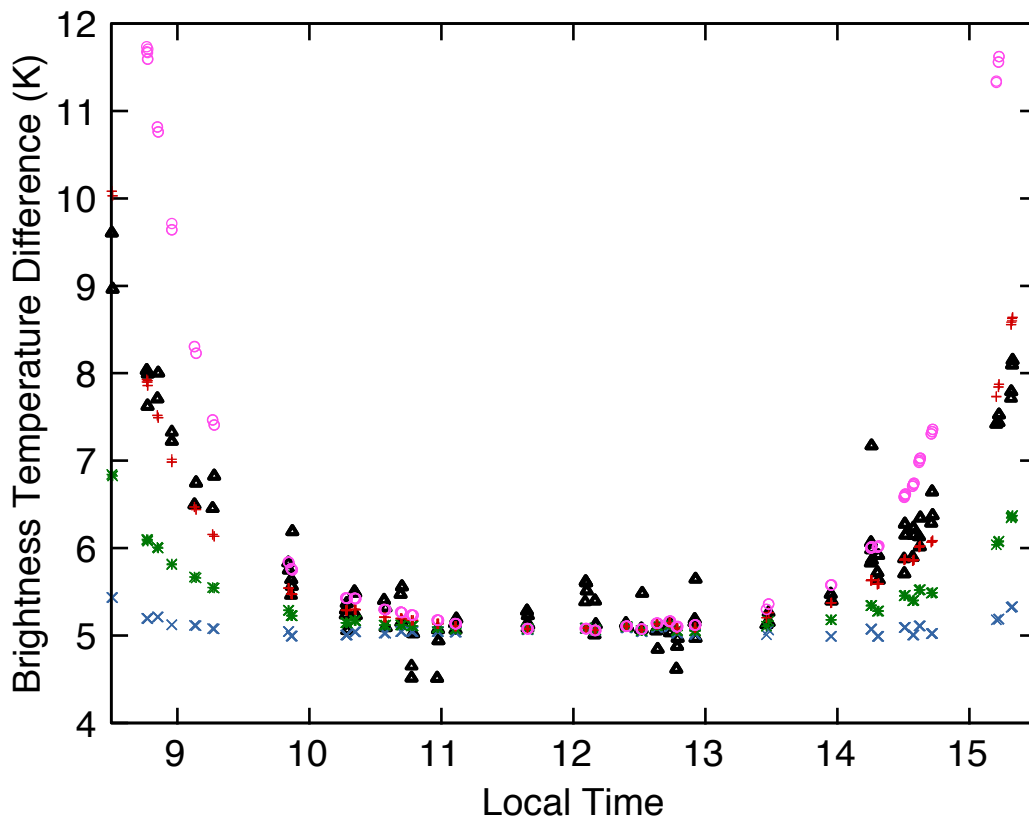
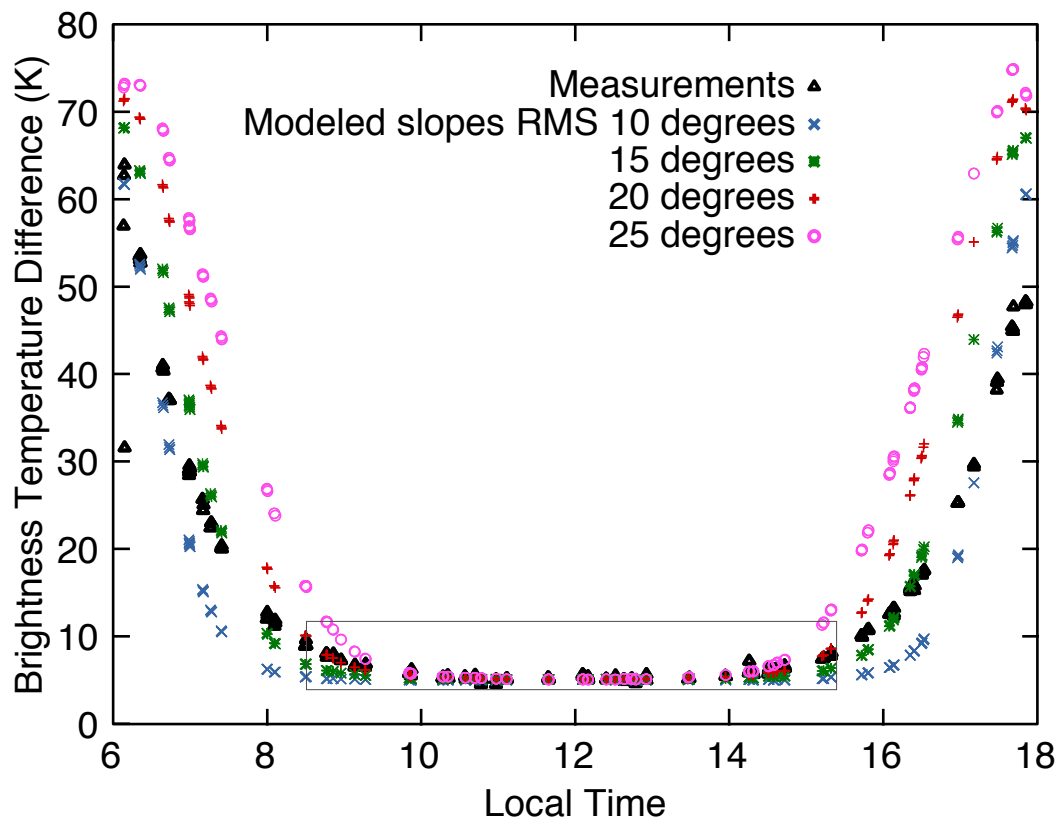


Figure 6. Diviner Channel 4 (8.2 μm) minus Channel 7 (25–41 μm) brightness temperature differences for nadir-oriented measurements for the mare region of interest used in this study (black triangles). Modeled Diviner brightness temperature differences for RMS slopes of 10, 15, 20, and 25° are also shown. The bottom plot shows a subset of the data designated by the rectangle in the top plot.

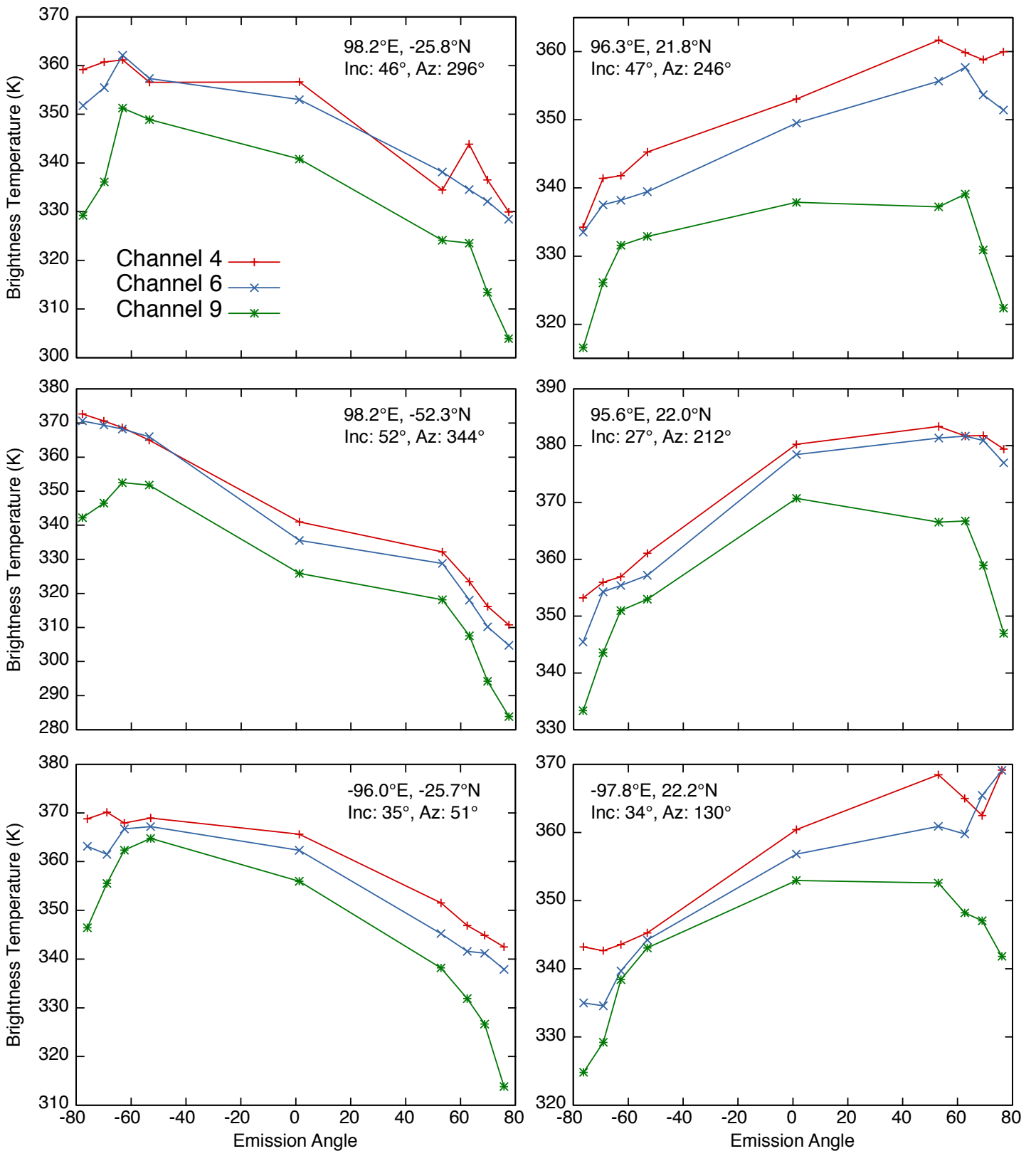


Figure 7. Diviner daytime emission phase function measurements for Channels 4, 6, and 9 (8.2, 13–23, and 100–300 μm). Each observation set (Table 2) includes measurements made from the north (negative emission angles), nadir, and from the south (positive emission angles). Inc and Az are the solar incidence and azimuth (degrees clockwise from north) respectively for each observation set.

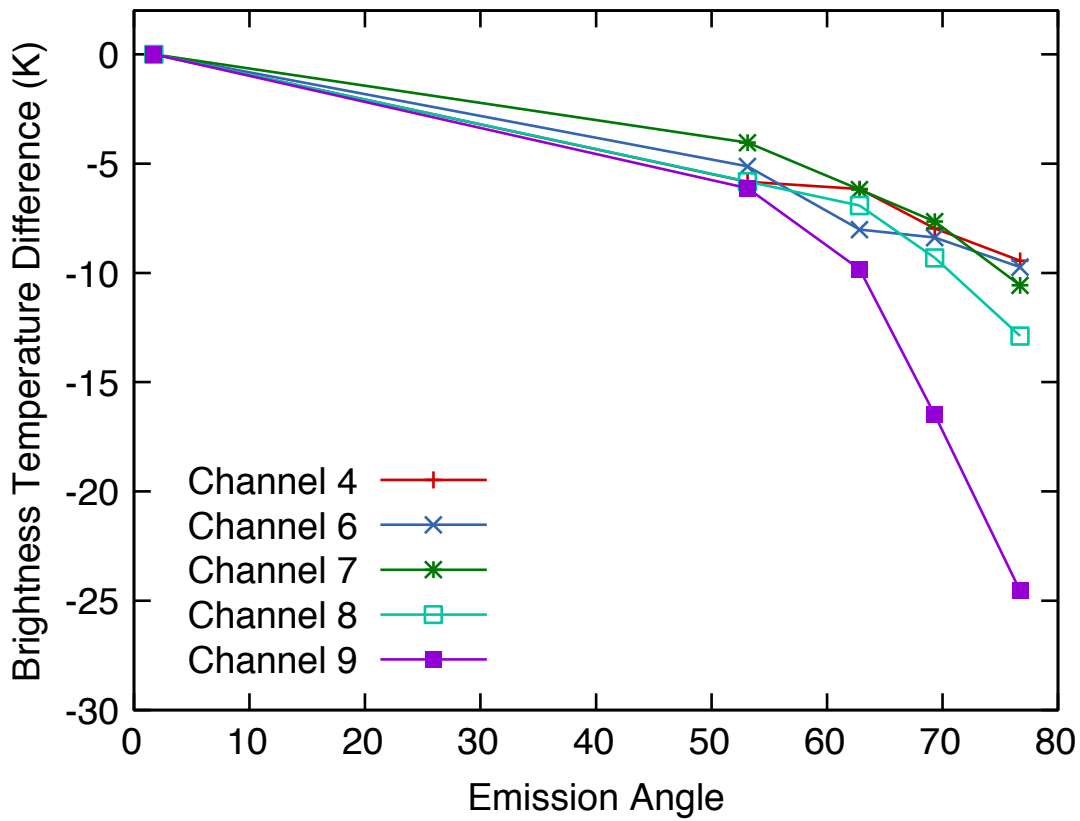


Figure 8. Decline in brightness temperature as a function of emission angle relative to the nadir-oriented observation. Data are taken from the average of all daytime emission phase function observations listed in Table 2. Diviner Channels 3 and 5 are not shown for clarity, but follow a pattern similar to that of Channel 4. Observations include averages of both poleward- and equatorward-facing observations (distinguished by positive and negative emission angles in Figure 7), which largely cancels out roughness effects that are azimuth dependent.

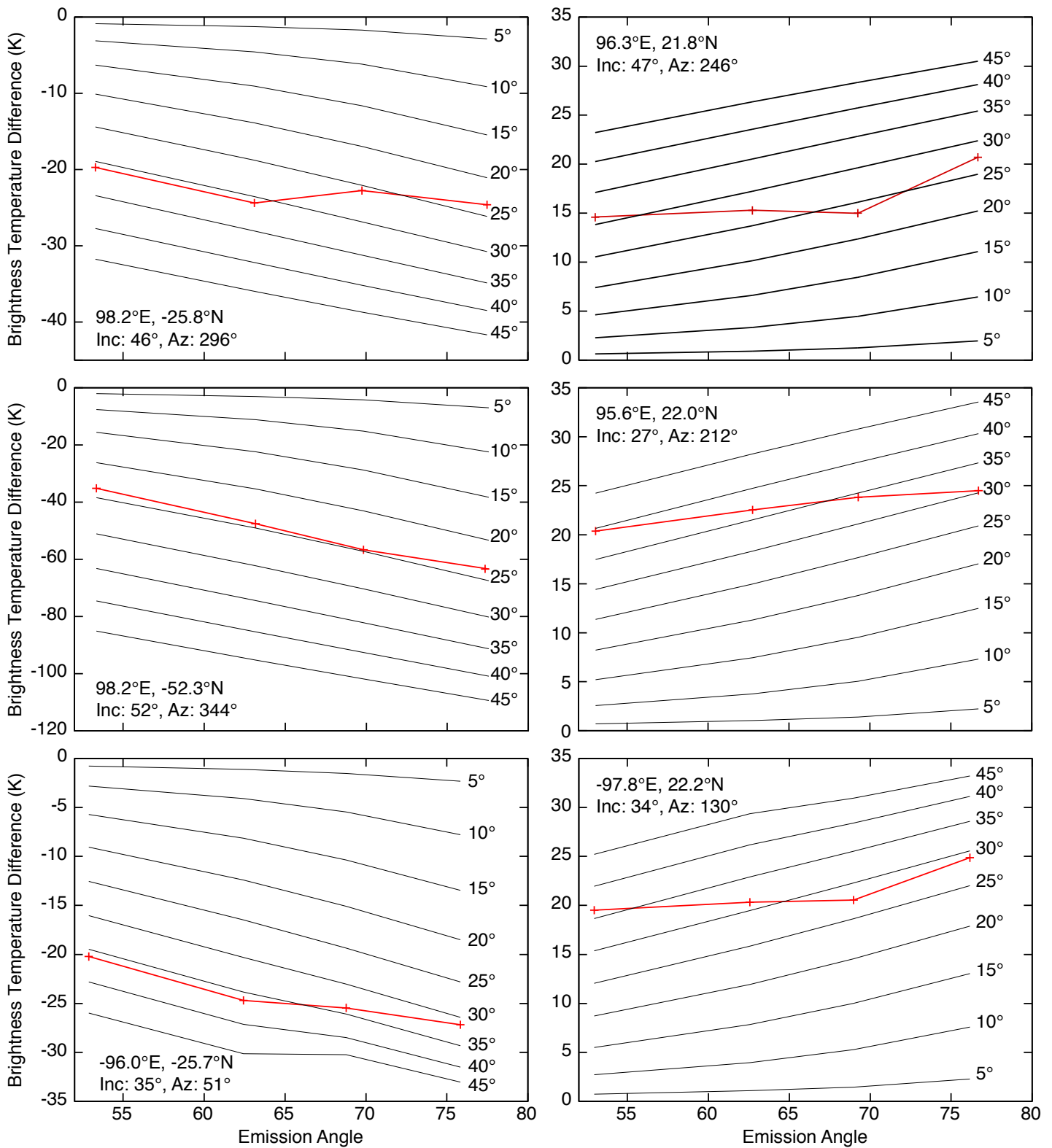


Figure 9. Comparison of Diviner daytime emission phase function observations (red symbols and lines) to RMS roughness models with mean slopes of 5–45° (black lines). Data and models are an average of all Diviner spectral channels. The brightness temperatures in the plots represent the difference between opposing north- and south-facing emission angle observations. Inc and Az are the solar incidence and azimuth (degrees clockwise from north) respectively for each observation set.

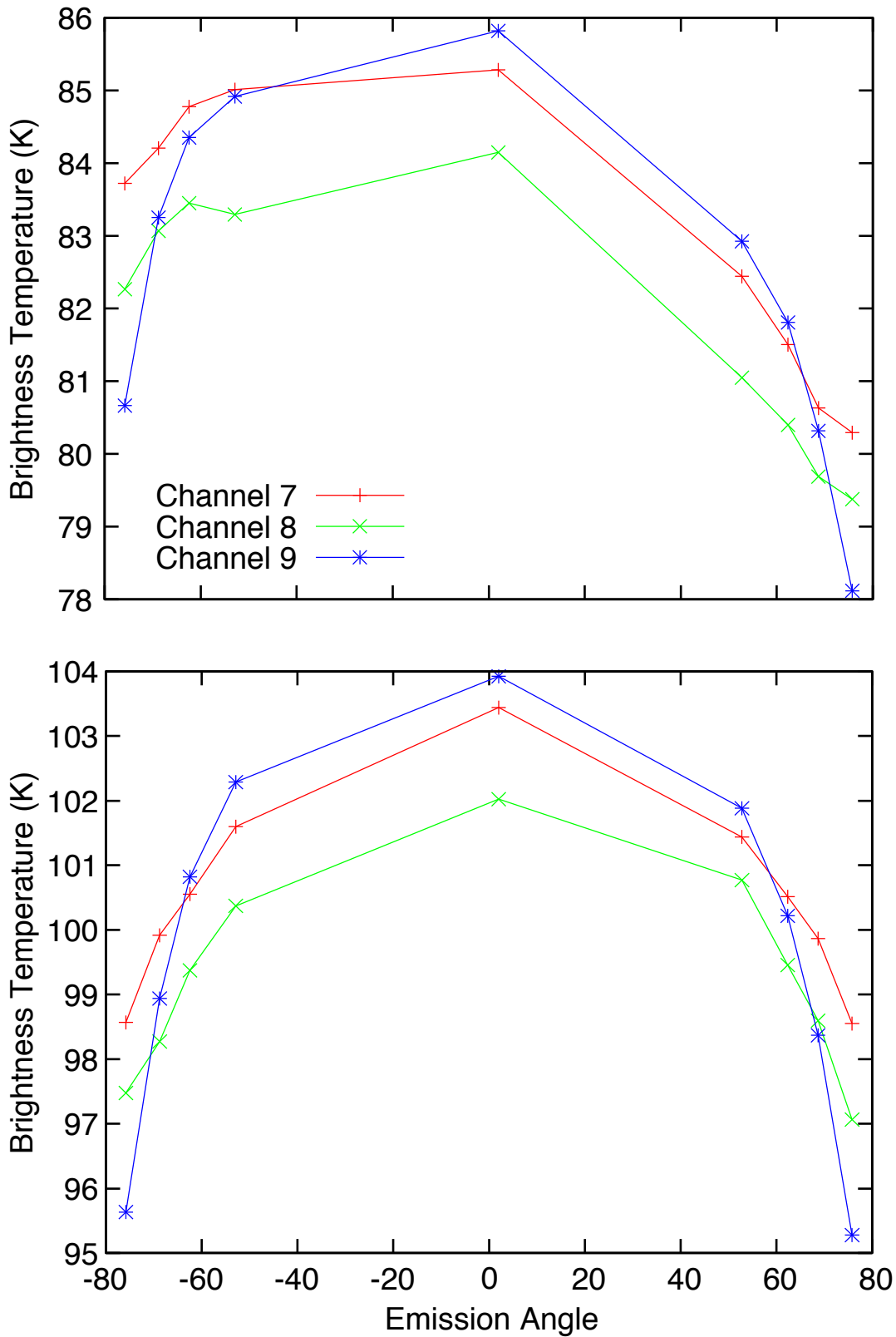


Figure 10. Average brightness temperatures for nighttime emission phase function observations at latitudes poleward of 50° latitude (top) and equatorward of 50° (bottom). Negative emission angles correspond to viewing angles from the equatorward direction and positive emission angles correspond to viewing angles from the poleward direction.

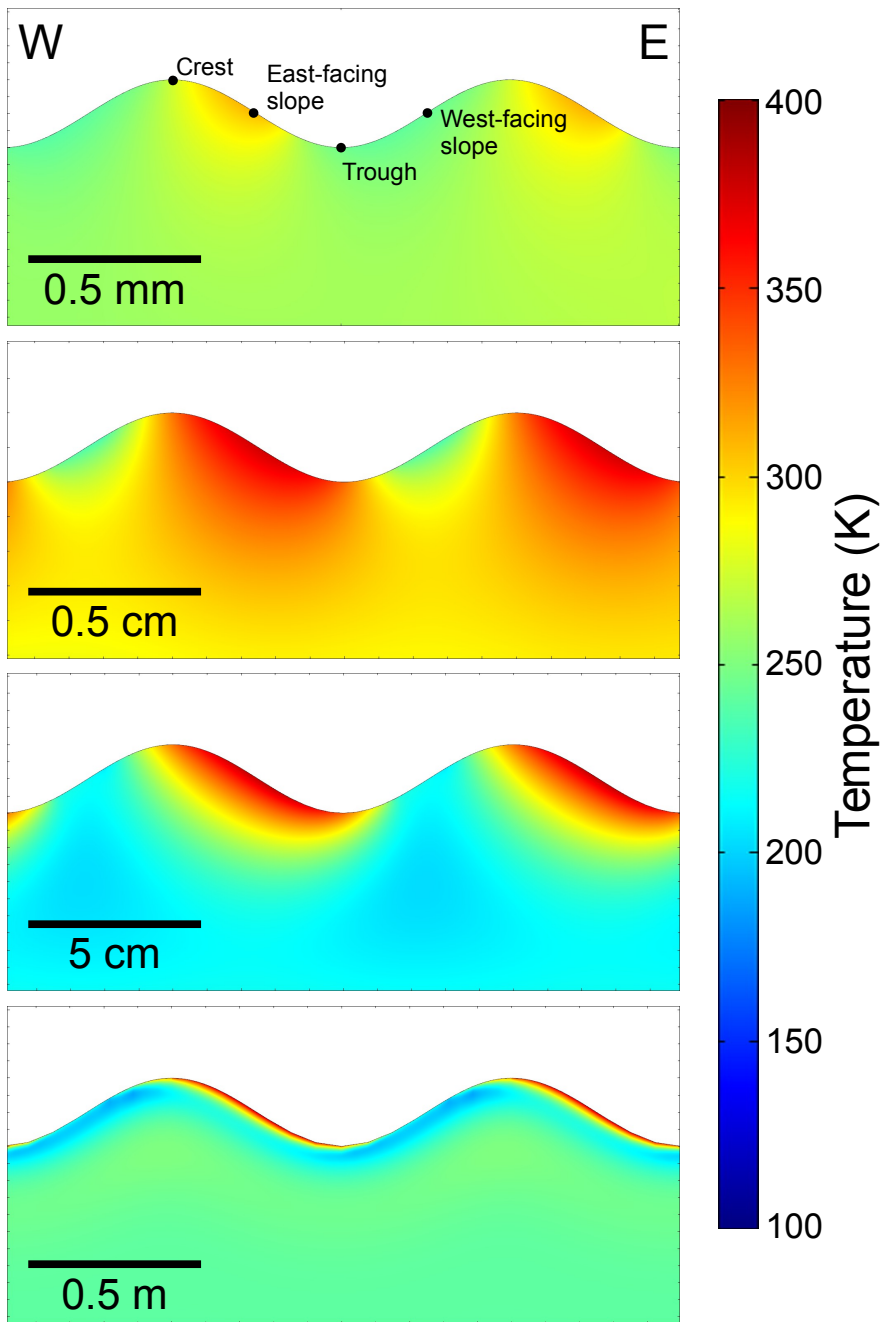


Figure 11. 2-dimensional temperature model results for a local time of 0800H with the sun in the east at an incidence of 60° . Each image shows an east-west trending cross section for the 4 separate length scales that were investigated. Specific surfaces discussed in Figures 12 and 13 are labeled in the top cross section.

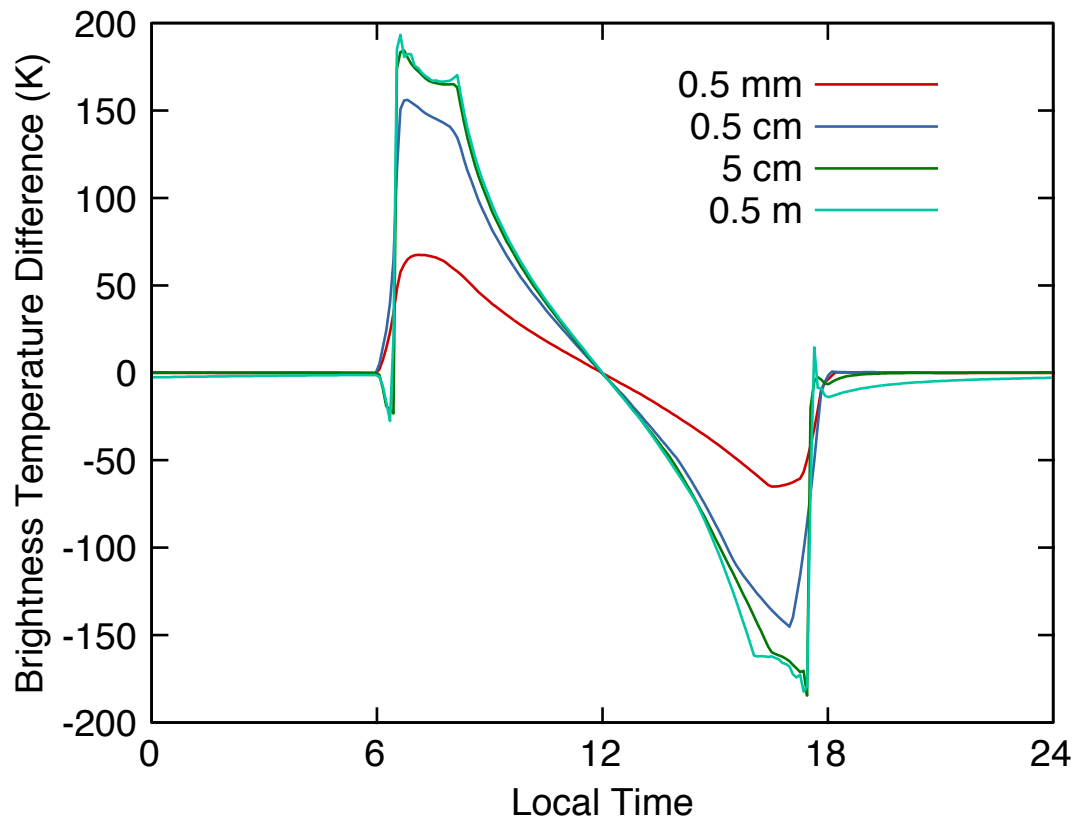


Figure 12. Temperature differences between the east- and west- facing slopes (denoted in Figure 11) for the 4 length scales as a function of local time. Smaller length scales are unable to remain as thermally isolated as the larger scale features.

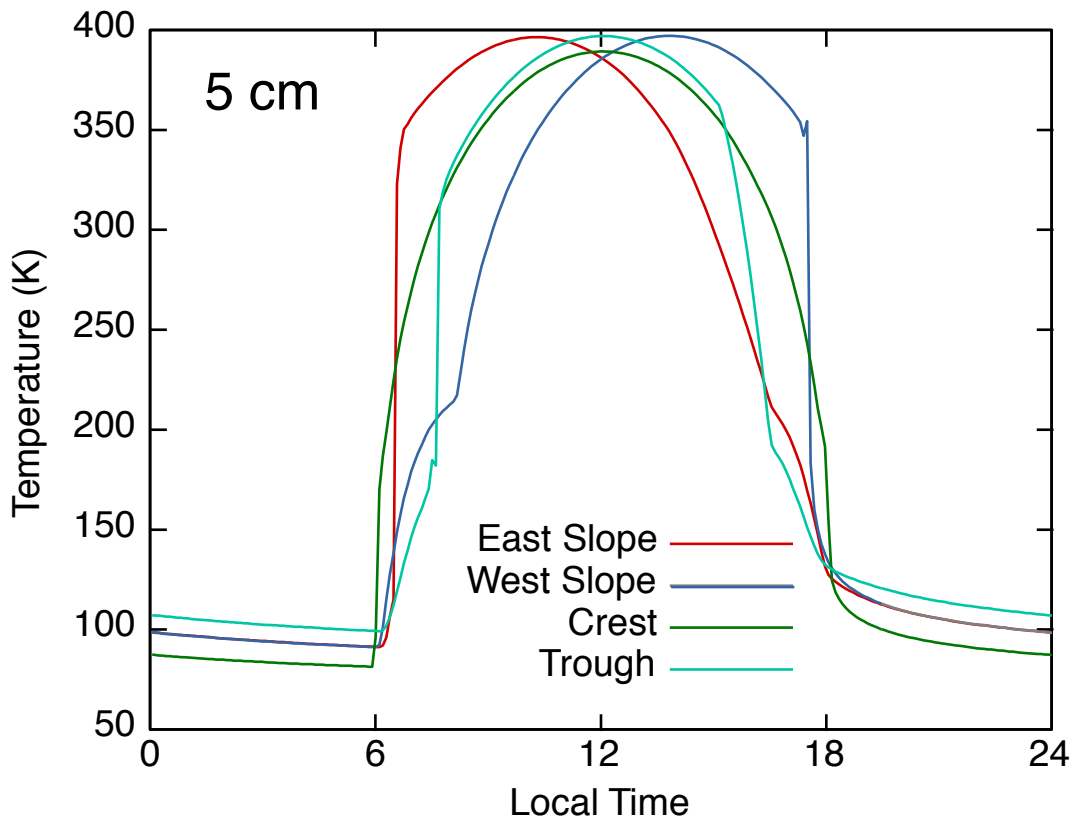
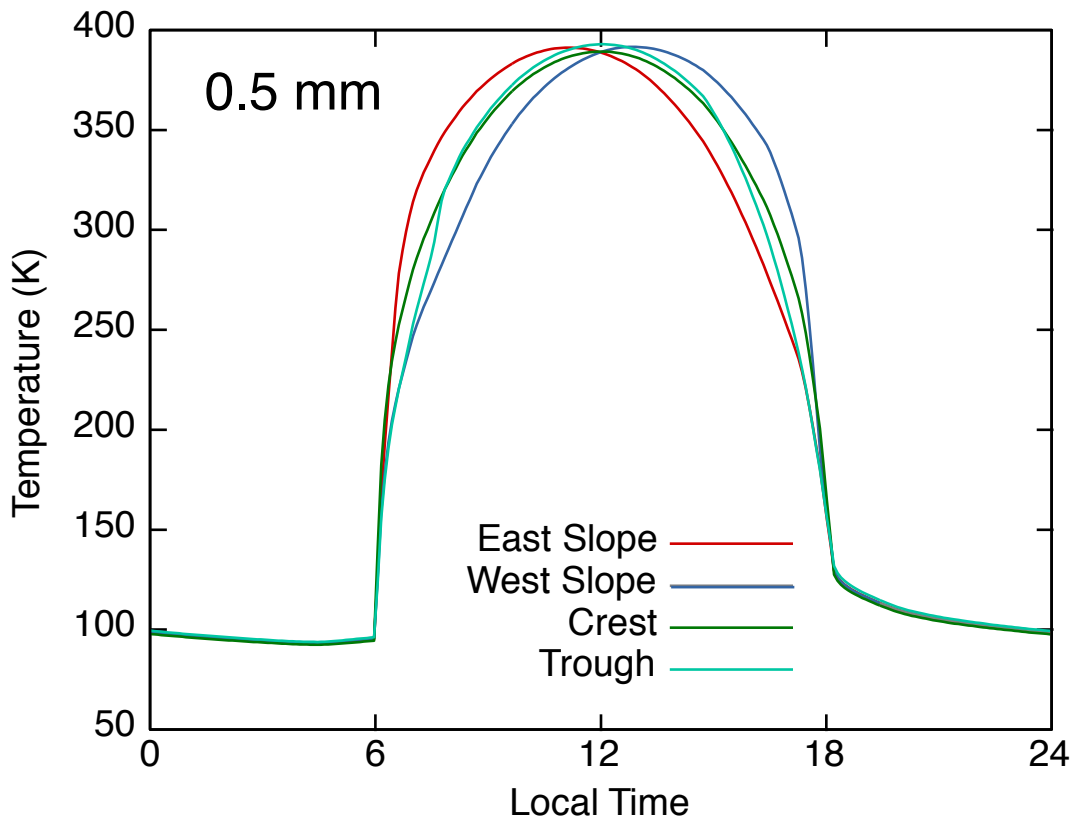


Figure 13. Surface temperatures for the east- and west-facing slopes, crest, and trough surfaces denoted in Figure 11. Two length scales are shown; 5cm, where the four surfaces remain thermally isolated, and 0.5mm, where the thermal isolation is significantly reduced.



Figure 14. Apollo image AS15-82-11155 showing several lunar regolith textures; undisturbed regolith, a rake sample collection site indicated by the parallel linear ridges, and compressed and smoothed regolith that is present within the astronaut boot prints.

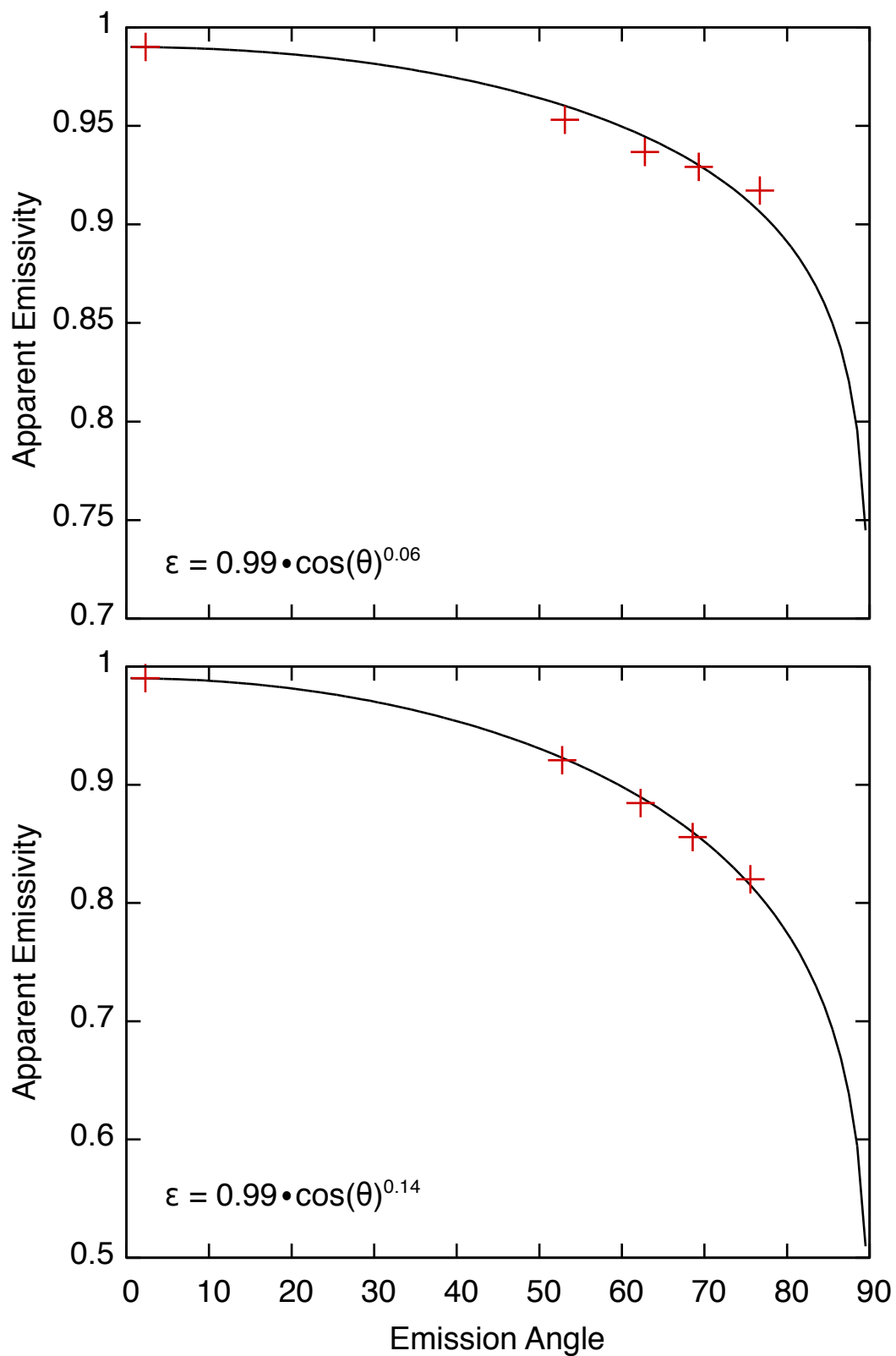


Figure 15. Diviner broadband apparent emissivity as a function of emission angle (red crosses) for daytime (top) and nighttime (bottom) emission phase function observations. Nadir emissivity is assumed to be 0.99. The equations (black lines) are fits to the data used to calculate hemispherical emissivity discussed in the text.